Article

Binding of IFT22 to the intraflagellar transport complex is essential for flagellum assembly

Stefanie Wachter[1], Jamin Jung[2], Shahaan Shafiq[2], Jerome Basquin[1], Cécile Fort[2], Philippe Bastin[2] (iD) &
Esben Lorentzen[3,*] (iD)

Abstract

Intraflagellar transport (IFT) relies on motor proteins and the IFT complex to construct cilia and flagella. The IFT complex subunit IFT22/RabL5 has sequence similarity with small GTPases although the nucleotide specificity is unclear because of non-conserved G4/G5 motifs. We show that IFT22 specifically associates with G-nucleotides and present crystal structures of IFT22 in complex with GDP, GTP, and with IFT74/81. Our structural analysis unravels an unusual GTP/GDP-binding mode of IFT22 bypassing the classical G4 motif. The GTPase switch regions of IFT22 become ordered upon complex formation with IFT74/81 and mediate most of the IFT22-74/81 interactions. Structure-based mutagenesis reveals that association of IFT22 with the IFT complex is essential for flagellum construction in *Trypanosoma brucei* although IFT22 GTP-loading is not strictly required.

Introduction

Cilia (also known as flagella) are important organelles needed for cell motility, morphogenesis, sensory perception, and several signaling pathways, such as sonic hedgehog and PDGFRα signaling (Huangfu *et al*, 2003; Kohl *et al*, 2003; San Agustin *et al*, 2015; Salinas *et al*, 2017; Schneider *et al*, 2005). Cilia are tail-like appendages protruding from the cell surface of nearly every eukaryotic cell type and are found on various unicellular organisms and on almost all cells in the mammalian body. For example, the protist *Trypanosoma brucei*, commonly known as the parasite causing sleeping sickness, carries a motile flagellum that is required for development and disease pathogenesis (Ralston *et al*, 2009; Langousis & Hill, 2014; Rotureau *et al*, 2014).

A microtubule-based axoneme extending from the centriole-like basal body at the ciliary base is the central shape-giving element of cilia. The organelle is surrounded by the ciliary membrane, which is a continuous outgrowth of the plasma membrane but hosts a unique composition of lipids and membrane proteins (Emmer *et al*, 2010; Serricchio *et al*, 2015). To date, more than 600 different proteins have been identified to reside in the ciliary compartment (Pazour *et al*, 2005). Cilia construction as well as maintenance of the organelle in almost all organisms relies on a conserved active transport process termed intraflagellar transport (IFT; Kozminski *et al*, 1993; Rosenbaum & Witman, 2002). Intraflagellar transport particles are thought to be responsible for the selective transfer of ciliary cargo proteins from the cytoplasm through the diffusion barrier at the transition zone. IFT is dependent on the motor proteins kinesin II for anterograde (base to tip; Cole *et al*, 1993, 1998; Prevo *et al*, 2015) and dynein 2 for retrograde (tip to base) movement (Pazour *et al*, 1999; Porter *et al*, 1999; Signor *et al*, 1999) of cargo proteins and turnover products. The IFT complex is required for construction of the flagellum and likely serves important functions in ciliary cargo selection and transport (Bhogaraju *et al*, 2013b) and can be divided into biochemically distinct IFT-A and IFT-B sub-complexes, consisting of 6 and at least 16 individual proteins, respectively (Piperno & Mead, 1997; Cole *et al*, 1998; Taschner & Lorentzen, 2016b). The IFT-B complex is organized into two stable sub-complexes, the 10-subunit IFT-B1 (IFT22, IFT25, IFT27, IFT46, IFT52, IFT56, IFT70, IFT74, IFT81, IFT88; Lucker *et al*, 2005; Follit *et al*, 2009; Ishikawa *et al*, 2014; Taschner *et al*, 2014) and the 6-subunit IFT-B2 complex (Taschner *et al*, 2016). While inactivation of IFT-B complex components or the kinesin motor typically leads to defects in cilium construction due to disrupted anterograde IFT (Pazour *et al*, 2000; Absalon *et al*, 2008), IFT-A protein or dynein deletions produce phenotypes associated with malfunctioning retrograde transport (Pazour *et al*, 1999; Blacque *et al*, 2006). Mutations in IFT components and other ciliary proteins are the cause for a wide range of genetic diseases and developmental abnormalities, known as ciliopathies (Reiter & Leroux, 2017).

For the assembly of large complexes that bind diverse cargo proteins, most IFT proteins are composed of protein–protein interaction domains such as coiled-coils, β-propellers, and tetratricopeptide

---

1 Department of Structural Cell Biology, Max Planck Institute of Biochemistry, Martinsried, Germany
2 Trypanosome Cell Biology Unit, Institut Pasteur & INSERM U1201, Paris, France
3 Department of Molecular Biology and Genetics, Aarhus University, Aarhus C, Denmark
*Corresponding author. Tel: +45 87155478;; E-mail: el@mbg.au.dk

repeats (Taschner *et al*, 2012). However, the two IFT complex members IFT22 (Rabl5) and IFT27 (Rabl4) show significant sequence homology to small GTPases of the Rab family, which are key regulators of vesicular membrane-trafficking (Stenmark, 2009; Itzen & Goody, 2011). IFT22 and IFT27 share low sequence identity (< 15%) and may play regulatory roles in IFT (Schafer *et al*, 2006; Qin *et al*, 2007; Adhiambo *et al*, 2009; Bhogaraju *et al*, 2011). In mammalian cilia, IFT27 was shown to be required for exit of the BBSome complex and associated ciliary cargoes (Keady *et al*, 2012; Eguether *et al*, 2014). Recently, Rabl2 was identified as a potential third Rab-like member of the IFT complex as it was shown to regulate IFT initiation and to associate with the IFT74/81 sub-complex (Lo *et al*, 2012; Kanie *et al*, 2017; Nishijima *et al*, 2017). Interestingly, IFT22 and IFT27 also associate with the IFT74/81 sub-complex (Taschner *et al*, 2014) suggesting that IFT22, IFT27, and Rabl2 may be located within close proximity in the IFT B1 complex. IFT22, IFT27, and RabL2 are unusual Rab GTPases as they lack the C-terminal prenylation motif commonly found to associate Rab GTPases with membranes.

Previous studies classified IFT22 as an atypical small GTPase with a high degree of sequence variance from classical Rab proteins, particularly in sequences assigned to the conserved nucleotide-binding pocket (Schafer *et al*, 2006; Adhiambo *et al*, 2009). IFT22 lacks the conventional G4 motif and contains a highly diverse G5 motif required for interaction with the guanine base of GTP/GDP (Rensland *et al*, 1995; Vetter & Wittinghofer, 2001; Itzen & Goody, 2011). Hence, it is unclear if IFT22 can specifically bind guanine nucleotides. Interestingly, *in vivo* studies in several ciliated organisms revealed functional differences of IFT22 between species. Mutation of the *Caenorhabditis elegans* (*Ce*) IFT22 homolog (called IFTA-2) does not affect cilium formation or IFT, but worms show deficiencies in the DAF-2 (insulin-IGF-1-like) signaling pathway, leading to an extended lifespan and abnormalities in dauer stage formation (Schafer *et al*, 2006; Blacque *et al*, 2018). In contrast, RNAi knockdown experiments of IFT22/Rabl5 in *Trypanosoma brucei* (*Tb*) led to a retrograde IFT inactivation phenotype that is characterized by short flagella filled with IFT material (Adhiambo *et al*, 2009). In *Chlamydomonas reinhardtii* (*Cr*), IFT22 was shown to control the cellular levels of both IFT-A and IFT-B proteins and to regulate availability of particles participating in IFT (Silva *et al*, 2012). Intriguingly, IFT22 homologs are missing in the genomes of *Giardia intestinalis* and *Tetrahymena thermophila*, although IFT is present in these ciliated organisms, whereas *Drosophila melanogaster* lacks both IFT22 and IFT74/81 homologs (van Dam *et al*, 2013).

In this study, we provide insights into nucleotide specificity of IFT22, the molecular basis of incorporation into the IFT complex and a dissection of the *in vivo* function of IFT22 using structure-based mutations in *T. brucei*. We show that IFT22 specifically binds G-nucleotides and present the crystal structures of GTP- and GDP-bound IFT22, which identify a new, unusual binding mode for G-nucleotides in the absence of the classical G4 motif. The crystal structure of the trimeric IFT22/74/81 complex provides a molecular basis for IFT22 incorporation to the IFT complex via the switch regions of IFT22 and a heterodimeric coiled-coil region of IFT74/81. *In vivo* experiments using structure-based IFT22 mutants in *T. brucei* demonstrate that association of IFT22 with IFT-B1 is essential for ciliogenesis.

Results

IFT22 specifically binds GDP/GTP

Due to the unusual G4/G5 regions, it was unclear if IFT22 is a selective guanine nucleotide-binding protein or if IFT22 may bind other purine nucleotides such as ATP (Espinosa *et al*, 2009; Taschner *et al*, 2012). To address nucleotide specificity, we overexpressed and purified *Tb*IFT22 and removed nucleotides retained during the purification by urea treatment and refolding (Appendix Fig S1A–C). We then measured the affinities of apo *Tb*IFT22 for GTP and GDP in titration experiments with fluorescently labeled non-hydrolyzable GTP/ATP derivatives (mant-GMPPNP/mant-AMPPNP) or GDP (mant-GDP). *Tb*IFT22 bound the GTP analog with a K_d of 2 μM and GDP with a K_d of 20 μM (Fig 1A, left and middle panels). These weak μM affinities are in the same range as reported for GTP/GDP-binding by IFT27 (Bhogaraju *et al*, 2011) and suggest that nucleotide exchange does not necessarily require a guanine nucleotide exchange factor (GEF), as it is the case for some large GTPases (Uthaiah *et al*, 2003). No binding was observed for the ATP analog (Fig 1A, right panel). We therefore conclude that IFT22 is a specific guanine nucleotide-binding protein.

We also measured the affinities for mant-GMPPNP and mant-GDP of IFT22 in context of the *Tb*IFT22/74/81 core complex (TbIFT22/74$_{342-401}$/81$_{397-450}$), which demonstrated a modest increase in affinities when compared to IF22 alone (Fig 1A, left and middle panels). To confirm these results, IFT22 or IFT22/74/81 core complexes from *Tb*, *M. musculus* (*Mm*) or *C. reinhardtii* (*Cr*) were incubated with excess of GTP and the content of bound nucleotides analyzed after size-exclusion chromatography (SEC) using an HPLC-based system (Appendix Fig S1E). IFT22/74/81 core complexes from all three species bound GTP, albeit to a different degree. The core complex from *T. brucei* incorporated the highest percentage of GTP, followed by *C. reinhardtii* and last *M. musculus*. Notably, *Tb*IFT22 bound less GTP than the *Tb*IFT22/74/81 core complex and no nucleotide could be detected for *Mm*IFT22, which likely reflects that *Mm*IFT22 has lower affinity for GTP than the *Tb* and *Cr*IFT22 proteins. These results show that GTP-binding is a conserved property of IFT22 across species and confirm that the IFT22/74/81 core complex has higher affinity for GTP than IFT22 alone.

Next, we analyzed the intrinsic GTPase activity of *Tb*IFT22 and detected very low but measureable hydrolysis rates for both *Tb*IFT22 and the *Tb*IFT22/74/81 core complex (Appendix Fig S1F) comparable to reported intrinsic hydrolysis rates of other small GTPases (Simon *et al*, 1996; Scheffzek & Ahmadian, 2005; Bhogaraju *et al*, 2011). Thus, if GTP turnover is required for the cellular function of IFT22, a GTPase activating protein (GAP) is required to stimulate nucleotide hydrolysis.

Structures of IFT22 with GTP or GDP reveal the molecular basis of guanine specificity

To address the molecular basis of nucleotide binding by IFT22, we crystallized *Tb*IFT22 with co-purified GTP and determined the structure at 2.3 Å resolution (Fig 1B and Table 1). To obtain a GDP-bound structure, *Tb*IFT22 was treated with urea, dialyzed to remove bound nucleotides, and refolded in the presence of GDP. The IFT22-GDP structure was determined at 2.5 Å resolution, and
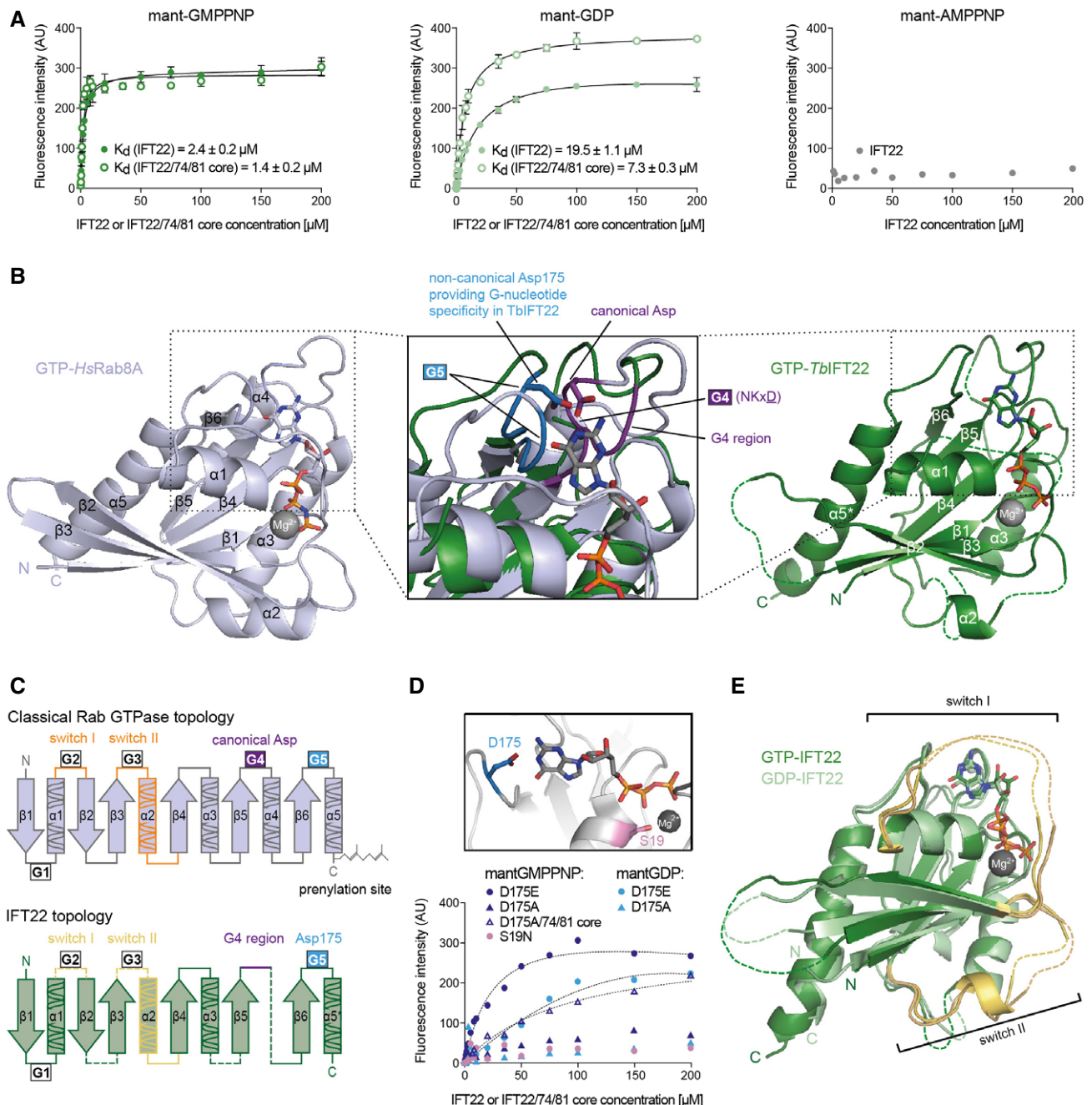
Figure 1. IFT22 associates with guanine nucleotides through an unusual G5-dependent mechanism.

A   IFT22 nucleotide-binding experiments. Fluorescence measurements using increasing amounts of *Tb*IFT22 and *Tb*IFT22/74$_{342–401}$/81$_{397–450}$ core complex incubated with mant-labeled GDP (mant-GDP) or non-hydrolysable GTP/ATP analogs (mant-GMPPNP/mant-AMPPNP). The fluorescence intensity is plotted as a function of protein concentration. Data were fitted to a single-site binding equation for determination of the dissociation constant (K_d). K_d values and standard deviations are calculated from three independent experiments.

B   Structural comparison of GTP-bound *Hs*Rab8A (light purple) and *Tb*IFT22 (green) depicted in cartoon representation. Nucleotides are shown as sticks and Mg^{2+} as balls. Unstructured regions of *Tb*IFT22 are represented with dotted lines. The zoomed-in view shows a superposition of the nucleotide-binding pocket. While classical GTPases form hydrogen bonds between a conserved aspartate of the G4 motif (NKxD) and the guanine base, IFT22 instead utilizes D175 located in the G5 loop.

C   Topology diagrams of a classical Rab GTPase and of IFT22. Positions of the conserved nucleotide-binding G-motifs (G1–G5) as well as switch regions are indicated.

D   Top: Cartoon representation of IFT22 (gray) with positions of two nucleotide-binding mutants highlighted. GTP is shown in stick representation and Mg^{2+} as a ball. D175 (blue) is the unusual residue binding the guanine base (see also Fig 1B), while S19 (pink) is a conserved residue required for coordination of the Mg^{2+} cation and is commonly mutated to an asparagine to prevent nucleotide binding. Bottom: Nucleotide-binding experiments of IFT22 nucleotide-binding mutants D175E, D175A, and S19N with fluorescently labeled nucleotides. Only the S19N mutation (light pink) abolished IFT22 nucleotide-binding ability completely.

E   Superposition of GTP (green)- and GDP-bound (light green) *Tb*IFT22 structures. Switch regions are marked in yellow and dotted lines indicate disordered loops not modeled in the structures.

the electron density clearly supports the presence of GDP (Appendix Fig S1G, compare left and middle panels). As expected, IFT22 exhibits the overall fold of a Rab GTPase, containing a mixed six-stranded β-sheet surrounded by α-helices (Fig 1B, right image). However, in contrast to classical GTPases that contain five α-helices, IFT22 lacks the α4 helix between β5 and β6 (Fig 1C). When the IFT22 structure is compared to protein structures currently available in the protein data bank using the Dali server (Holm & Sander, 1993), IFT22 is most similar to structures of other Rab family GTPases with *Homo sapiens (Hs)* Rab8A as the closest match (PDB ID: 4lhw), superposing with a root mean square deviation (rmsd) of 2.4 Å (see Fig 1B).

The high degree of sequence divergence of IFT22 when compared to other Rab GTPases (Appendix Fig S2) translates into a highly unconventional nucleotide-binding mode in IFT22. The classical G4 NKxD motif, which is missing in IFT22, features an aspartate residue (D124 in *Hs*Rab8A, see Fig 1B, detailed view) that interacts with the base of the nucleotide thus providing specificity for guanine over adenine (Rensland *et al*, 1995; Paduch *et al*, 2001). In the absence of a G4 aspartic acid, *Tb*IFT22 uses D175 from the unusual G5 motif to form a bifurcated hydrogen bond with the guanine moiety (see detailed view in Fig 1B). While the classical G4 motif is positioned in a loop connecting β5 with α4, Asp175 is located between β6 and α5* (see Fig 1C). IFT22 homologs from *D. rerio (Dr)* and mammals (*Mm, Hs*) have a glutamate residue in the position of *Tb*IFT22 D175 (Appendix Fig S2) indicating a potentially similar binding mechanism in those species. *Cr* and *C. elegans (Ce)* IFT22 contain an alanine and a glycine, respectively, at the position of *Tb*IFT22 D175 making it unclear how or if they achieve specificity for G-nucleotides.

Table 1. Data collection and refinement statistics.

	*Tb*IFT22-GTP	*Tb*IFT22-GDP	*Tb*IFT22/74$_{79-401}$/81$_{1-450}$-GTP (SeMet)
PDB code	6IA7	6IAE	6IAN
Data collection			
Wavelength (Å)	1.00000	0.97891	0.97899
Resolution range (Å)	48.37–2.30 (2.38–2.30)	48.52–2.49 (2.57–2.49)	82.67–3.20 (3.40–3.20)
Space group	P 61	P 61	P 21
Unit cell (Å, °)	a = 55.85	a = 56.02	a = 68.56
	b = 55.85	b = 56.02	b = 228.30
	c = 263.45	c = 263.09	c = 115.71
	α = 90	α = 90	α = 90
	β = 90	β = 90	β = 96.76
	γ = 120	γ = 120	γ = 90
Total reflections	205,477 (17,635)	321,430 (27,213)	2,191,763 (226,031)
Unique reflections	20,689 (1,996)	16,300 (1,558)	113,747 (18,991)
Multiplicity	9.9 (8.8)	19.7 (17.5)	19.3 (11.9)
Completeness (%)	99.7 (96.7)	99.3 (96.1)	100.0 (100.0)
Mean I/sigma	16.7 (0.9)	18.5 (0.9)	11.5 (0.7)
CC1/2	0.999 (0.497)	0.998 (0.363)	0.999 (0.395)
Refinement			
Number of reflections	20,588	16,236	57,455
Protein residues	295	305	1,637
Number of atoms	2,311	2,354	12,090
R-work	0.212 (0.292)	0.220 (0.359)	0.241 (0.441)
R-free	0.264 (0.349)	0.244 (0.385)	0.280 (0.447)
Ramachandran favored (%)	93.5	94.0	96.3
Ramachandran outliers (%)	0.0	0.35	0.25
RMS bonds (Å)	0.005	0.006	0.007
RMS angles (°)	0.90	1.0	1.1
Average B-factors (Å^2)	64	72	143

Statistics for the highest resolution shell are shown in parentheses.

To evaluate the importance of D175 in GTP/GDP-binding, we purified D175E and D175A mutant forms of *Tb*IFT22 and carried out titrations with mant-GMPPNP or mant-GDP (Fig 1D). While the *Tb*IFT22$_{D175A}$ mutant did not show any detectable nucleotide-binding, the *Tb*IFT22$_{D175E}$ mutant bound mant-GMPPNP and mant-GDP with K$_D$ values of 18 μM and 139 μM, respectively, which is approximately one order of magnitude lower affinity than wild-type *Tb*IFT22. Interestingly, *Tb*IFT22$_{D175A}$ did bind mant-GMPPNP when in context of the IFT22$_{D175A}$/74/81 core complex with a K$_D$ of 102 μM, which is approximately two orders of magnitude lower affinity than what we observed for the wild-type IFT22/74/81 core complex (Fig 1A and D). These results are in agreement with higher GTP affinity of the IFT22/74/81 core complex compared to IFT22 alone. Our data demonstrate that D175 is important for nucleotide binding in *Tb*IFT22 and suggest that E175 can contact the guanine moiety of GTP/GDP although in a less favorable manner than D175 likely due to steric problems caused by the longer side-chain. We also introduced the classical S19N mutation in *Tb*IFT22 that prevents Mg^{2+} coordination and thus abolishes nucleotide binding. As expected, our titration data show that *Tb*IFT22$_{S19N}$ does not associate with mant-GMPPNP (Fig 1D).

A hallmark of small GTPases are the switch regions that typically undergo major conformational changes between the active GTP-bound and the inactive GDP-bound states, which allow for binding of effectors (Vetter & Wittinghofer, 2001; Mourão *et al*, 2014). Surprisingly, no major conformational changes were observed when comparing the GTP- and GDP-bound states of IFT22 and the switch regions are unstructured in both GDP- and GTP-bound *Tb*IFT22 structures (Fig 1E). While switch I and II of GDP-bound GTPases are known to be rather flexible and often unstructured, active GTP-bound forms usually exhibit ordered switch regions that provide a stable interaction surface for downstream effector binding. The switch regions of GTP-bound *Tb*IFT22 are thus not in a pre-ordered conformation ready to associate with effectors. However, the observation that the IFT22/74/81 core binds nucleotides with higher affinity than IFT22 alone does suggest that IFT74/81 may interact with and stabilize the nucleotide-binding pocket of IFT22.

Structure of the IFT22/74/81 complex

To elucidate how IFT22 is incorporated into the IFT-B1 complex and determine if IFT74/81 is an effector of IFT22, we set out to obtain a structure of IFT22/74/81. IFT74 and IFT81 are both predicted to contain mostly coiled-coil structures (Fig 2A) and share 26% sequence identity in *T. brucei* suggesting that IFT74 and IFT81 are distant homologs. IFT74 and IFT81 interact directly with each other to form a binding platform for the IFT-B1 components IFT22, IFT25/

27, and IFT46/52 (Lucker *et al*, 2005; Taschner *et al*, 2011, 2014). In addition to the coiled-coil regions, IFT74/81 contains an N-terminal tubulin-binding module contributed by both proteins (Bhogaraju *et al*, 2013a). Since IFT22/74/81 core complexes (*Tb*IFT22/74$_{342–401}$/81$_{397–450}$, Appendix Fig S1D) did not yield crystals, we co-expressed and purified longer constructs of *Tb*IFT74/81 with *Tb*IFT22, spanning the N-terminal predicted coiled-coil domains. The positively charged IFT74 N-terminus is prone to degradation and was consequently removed resulting in the *Tb*IFT74$_{79–401}$ construct. Whereas complexes lacking the IFT81 CH domain did not crystallize, the GTP-bound *Tb*IFT22/74$_{79–401}$/81$_{1–450}$ complex containing the IFT81 CH domain crystallized and the structure was determined at 3.2 Å resolution by experimental phasing (Appendix Fig S3A–C and Table 1).

The *Tb*IFT22/74$_{79–401}$/81$_{1–450}$ crystal structure reveals an elongated coiled-coil complex with the IFT81 CH domain and the IFT22 GTPase located at opposite ends (Fig 2B). Rather than forming one long coiled-coil, the IFT74$_{79–401}$/81$_{1–450}$ structure can be subdivided into six separate heterodimeric coiled-coil regions (ccI to ccVI) separated by short loop regions (Fig 2A and B). Boundaries of these coiled-coils do not match particularly well with predicted coiled-coils from the PCOILS webserver (Alva *et al*, 2016). IFT74 and IFT81 interact intimately and share a large buried surface interface of 8,300 Å^2, constituting both interactions within the coiled-coils and between different heterodimeric regions (Fig 2B and Appendix Fig S4). Whereas ccI and ccVI protrude from either end of the complex to interact with the IFT81 CH domain and IFT22, respectively, the central four coiled-coil regions, ccII-ccV, form a highly compact structure held together by interactions between ccII-ccIII, ccIII-ccIV, and ccII-ccIII-ccV (Appendix Fig S4). IFT74/81 ccII-ccV appears to form a rather unique compressed spring-like structure. Searches using the Dali server did not reveal any structures similar to IFT74/81 ccII-ccV in the protein data bank.

The position of the N-terminal IFT81 CH domain is fixed to IFT74/81 ccI through contacts with the 15-residue linker region and the bent C-terminal helix of the IFT81 CH domain (Appendix Fig S5E). This C-terminal helix, which is bent in IFT81 CH domains (Appendix Fig S5A and B), adopts a straight conformation in the two MT-binding CH domain containing proteins NDC80 and EB1 (Slep & Vale, 2007; Ciferri *et al*, 2008; Appendix Fig S5C and D). This observation provides a molecular rationale for the different architecture of the IFT74/81 and the NDC80/NUF2 complexes (Alushin *et al*, 2010; Appendix Fig S5F). Interestingly, many of the positively charged Arg/Lys residues previously shown to mediate αβ-tubulin cargo binding in the *Cr*IFT81 CH domain (Bhogaraju *et al*, 2013a) are found in structurally conserved positions in the *Tb*IFT81 CH domain (Fig 2C). These tubulin-binding residues point

►

Figure 2. Structure of the *Tb*IFT22/74/81 complex.

A Domain organization of IFT81, IFT74, and IFT22. Numbers refer to the *T. brucei* protein sequence and indicate different constructs used in this study. The part of the IFT81/74 sequence shown in shaded colors is not part of the construct used for structure determination. Coiled-coil boundaries are depicted based on the structure (ccI-ccVI) or prediction from the PCOILS webserver (cc). (CH = calponin homology, cc = coiled-coil).

B Crystal structure of *Tb*IFT22/74$_{79–401}$/81$_{1–450}$ in two perpendicular orientations shown in cartoon representation. GTP is shown as a stick model. IFT22 is depicted in green, IFT74 in orange, and IFT81 in gray. Coiled-coils are labeled ccI-ccVI.

C Zoomed-in view of the N-terminal *Tb*IFT81 CH domain (gray) superposed onto the *Cr*IFT81 CH domain (brick-red). Basic tubulin-binding residues are highlighted in yellow and light orange, respectively.

D Zoomed-in view of the IFT22-binding site on IFT74/81 ccVI with ordered switch regions of IFT22 depicted in yellow.
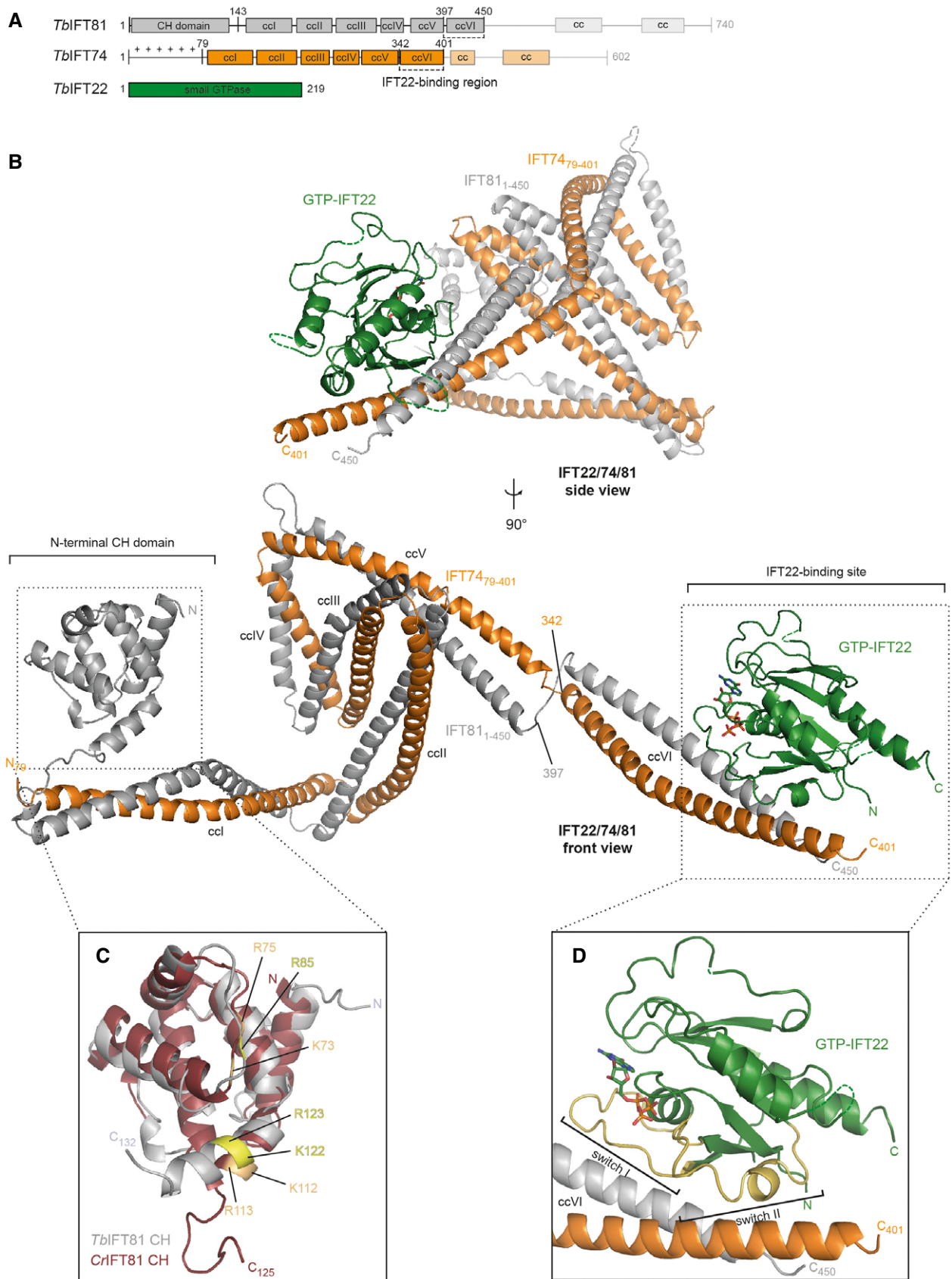
Figure 2

toward ccII-ccIV perhaps suggesting that tubulin cargo could be sandwiched in the gap between the CH domain and ccII-IV (Fig 2B and C).

Noteworthy, upon IFT74/81 association the switch regions of IFT22 become ordered and mediate binding to ccVI of IFT74/81 (Fig 2D). As observed for the IFT22/74/81 core complex, IFT22/74_{79-401}/81_{1-450} also co-purified with GTP (confirmed by HPLC) and was set up for crystallization with a molar excess of GTP at 4°C. Although the guanine base only displays partial electron density, the ribose and tri-phosphate moieties have clear electron density confirming that GTP is bound in the nucleotide-binding pocket of IFT22 (Appendix Fig S1G, right panel). The observation that the switch regions are ordered in the GTP-bound IFT22/74/81 complex structure but not in GTP-bound IFT22 shows that binding of IFT22 to IFT74/81 induces a fixed conformation of switch I and II (Fig 2D). There are no direct contacts between GTP and IFT74/81 suggesting that the increased nucleotide affinity of the IFT22/74/81 core complex compared to IFT22 alone (Fig 1A and E) is an indirect effect of fixing the switch regions in a conformation with higher nucleotide affinity.

The switch regions of IFT22 interact with a conserved surface patch contributed by both IFT74 and IFT81

Analysis of the TbIFT22/74/81 complex structure reveals a relatively small (710 Å^2 buried surface) mixed hydrophobic/hydrophilic interface of between IFT22 and IFT74/81 (Fig 3A and B). Switch I and II contribute most of the IFT22 residues to the interface with IFT74/81 with a few additional residues contributed from the β-sheet of the core GTPase fold (Fig 3B). Both IFT74 and IFT81 interact with IFT22 although IFT81 contributes about twice as many residues to the interface with IFT22 as IFT74 does (Fig 3A and B, and Appendix Fig S3D). A high degree of evolutionary conservation of residues in the interface between IFT22 and IFT74/81 (Fig 3A and Appendix Fig S3D) suggests that IFT22 associates with IFT74/81 in a similar manner in other ciliated organisms. To confirm this notion, we show that the IFT22-IFT74/81 interaction interface between *Chlamydomonas* and *Trypanosoma* is conserved to such a degree that TbIFT22 efficiently pulls down a purified CrIFT25/27/74/81 complex, thereby forming a stable pentameric IFT-B1 chimera (Fig 3C). The prevention of nucleotide-binding via the TbIFT22$_{S19N}$ mutant reduced the amount of CrIFT25/27/74/81 pulled down by His-tagged TbIFT22 to background levels (Fig 3C). We conclude that IFT22, using mainly switch I and II, interacts with IFT74/81 to form an evolutionarily conserved IFT-B sub-complex.

To verify the interaction observed in the IFT22/74/81 structure and devise mutants for *in vivo* analysis, we constructed 7 different point mutations of TbIFT22 residues and evaluated complex formation by co-expression and pull-down of the TbIFT22/74/81 core complex (Appendix Fig S3E). Two point mutations of well-conserved IFT22 residues abolished complex formation, namely R43E and A86R. R43 is located adjacent to switch I and A86 is located in switch II (highlighted in red in Fig 3C). Mutation of A86 to an arginine inserts a long, charged amino acid side-chain predicted from the structure to result in steric clashes with the IFT74 helix of ccVI and prevents complex formation with IFT74/81 (Fig 4D and Appendix Fig S3E). The R43 side-chain forms a salt bridge with E432 of IFT81 and the R43E charge reversal disrupts

core complex formation, whereas a R43A mutation leads to weaker binding without completely disrupting complex formation (Appendix Fig S3E). These results identify residues vital for the interaction of IFT22 with IFT74/81 and corroborate the interaction observed in the crystal structure (Fig 3).

IFT22 GTP-binding is not a strict requirement for IFT complex formation or *Trypanosoma* flagellum construction

Effectors preferably interact with the switch regions of the active GTP-bound state of small GTPases (Vetter & Wittinghofer, 2001), typically with three orders of magnitude higher affinity than with the GDP-bound state (Leung & Rosen, 2005). The IFT22/74/81 structure presented here demonstrates that GTP-bound IFT22 interacts with IFT74/81 mainly using the switch regions (Fig 3B), which suggests that IFT74/81 is an effector of IFT22. However, the fact that GDP- and GTP-bound TbIFT22, in the absence of IFT74/81, adopt very similar structures where switch I and II are disordered (Fig 1E) shows that GTP-bound IFT22 does not adopt a structure pre-ordered for IFT74/81-binding, but that the switch region conformation observed in the IFT22/74/81 structure is a result of an induced fit upon complex formation.

To further analyze the nucleotide requirement for IFT22 association with IFT74/81, we investigated different nucleotide-binding mutants (Fig 4). First, we examined the IFT22$_{D175A}$ mutant that binds GTP with about two orders of magnitude lower affinity than wild-type IFT22 (Fig 1D). Surprisingly, the wild-type and the IFT22$_{D175A}$ mutant pulled down similar amounts IFT74/81 (Fig 4A and B). However, as HPLC experiments showed that the IFT22$_{D175A}$/74/81 core complex still co-purified with GTP, we also tested the IFT22$_{S19N}$ mutant where Mg^{2+} binding is disrupted and GTP-binding completely abolished in our titration experiments (Fig 1D). TbIFT22$_{S19N}$ was unable to assemble into a core complex with TbIFT74$_{342-401}$/$81_{397-450}$ (Fig 4A) but could still interact to some degree with the TbIFT74$_{79-401}$/81_{1-450} complex used for structure determination (Fig 4B) and almost to the same level as wild-type IFT22 in case of the TbIFT25/27/74/81 complex (Fig 4C). These results may suggest that the helices of IFT74/81 ccVI are not stably associated in the absence of the C-terminal parts of IFT74/81. Indeed, we observed pronounced degradation of IFT81$_{1-450}$ in context of the IFT74$_{79-401}$/81_{1-450} complex when expressed in the absence of IFT22 (Appendix Fig S3F). We conclude that GTP-binding by IFT22 is not absolutely required for the interaction with IFT74/81 but appears to modulate the affinity of the interaction.

To examine the impact of the IFT22 nucleotide binding *in vivo*, a functional complementation assay was developed. RNAi knockdown of IFT22 in trypanosomes results in the assembly of short flagella accumulating IFT proteins as expected (Adhiambo *et al*, 2009). This phenotype was rescued by the expression of an RNAi-resistant version of IFT22 fused to GFP (GFP::IFT22$_{rescue}$) that localizes and traffics normally in the flagellum (for details, see supplemental text, Movies EV1 and EV2, and Appendix Fig S6). The IFT22$_{D175A}$ mutation was investigated in this context. Western blot analysis showed that GFP::IFT22$_{D175A}$ was expressed and resistant to silencing in contrast to the endogenous IFT22 protein (Appendix Fig S6C). IFT22$_{D175A}$ traffics normally in the flagellum in the presence (Movie EV3) and absence (Movie EV4) of the endogenous IFT22 protein. The fluorescent signal of GFP-IFT22$_{D175A}$ was
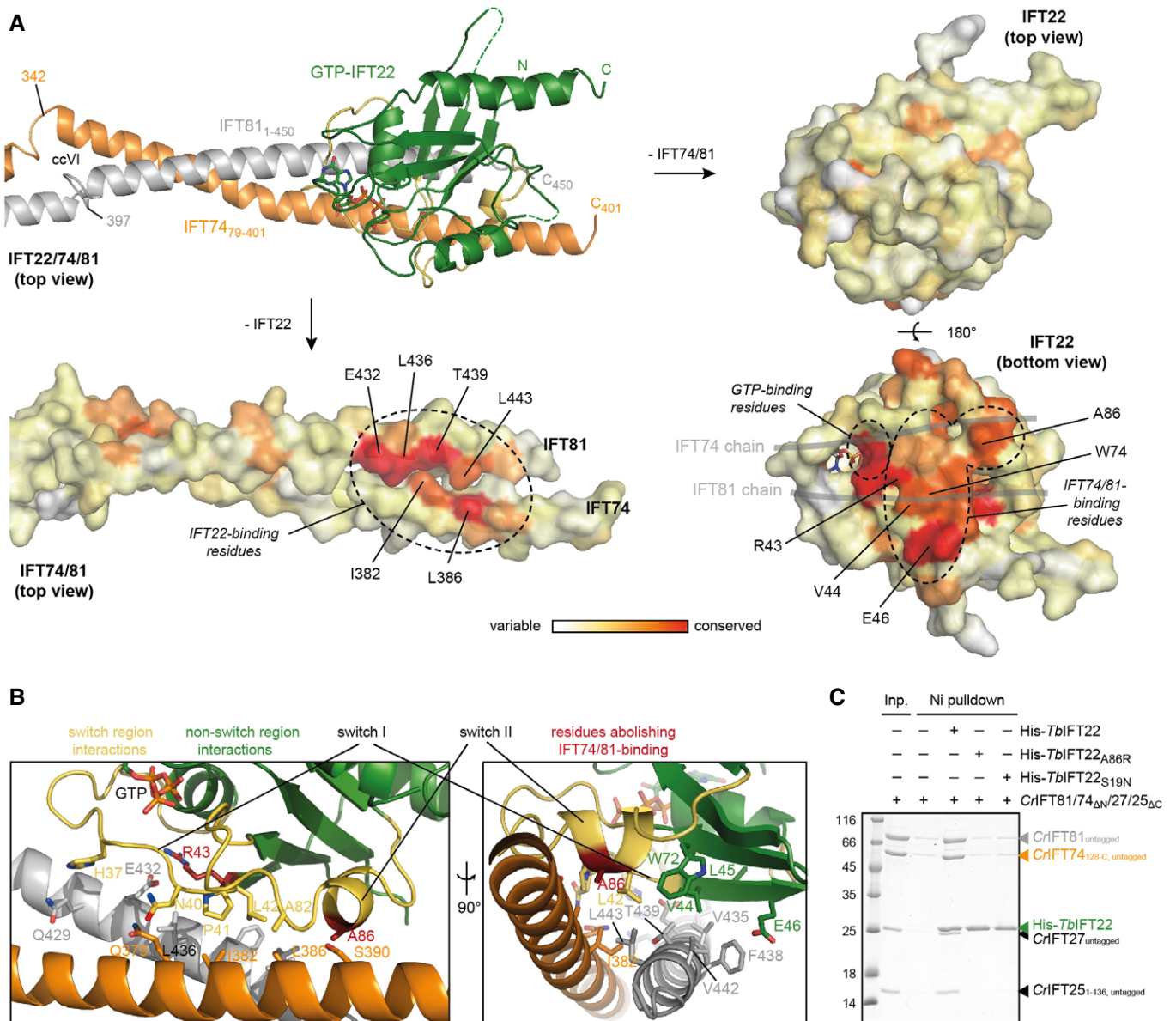
Figure 3. Molecular basis of IFT22 association with IFT74/81 ccVI.

A Cartoon representation of the IFT22-binding site on IFT74/81 ccVI (top left) and surface conservation representation of different orientations of IFT22/74/81 (top right and bottom). IFT74/81 ccVI displays a highly conserved patch at the IFT22-binding interface (black dashed circle). A 180° rotation of IFT22 (bottom right) exhibits a likewise conserved patch at the IFT74/81-binding interface (black dashed circles; position of the IFT74/81 helices is marked with light gray lines). Conserved residues are marked and labeled according to the *Tb* sequence. Conservation coloring is based on Clustal Omega multiple sequence alignments with *H. sapiens, M. musculus, D. rerio, T. brucei, C. reinhardtii,* and *C. elegans* sequences (see Appendix Fig S2 and Appendix Fig S3D) and ConSurf conservation grades (Landau *et al*, 2005; Sievers *et al*, 2011).

B Detailed view of the IFT22-IFT74/81 binding site in two perpendicular orientations showing interacting residues in stick representation. Residues provided by IFT22 switch I and II are shown in yellow, whereas IFT22 non-switch region interactions are colored in green. IFT74 is shown in orange and IFT81 in gray. IFT22 residue where mutation abolishes interaction with IFT74/81 are highlighted in red (R43 and A86, see also Fig 4 and Appendix Fig S3E).

C SDS–PAGE gel of a Ni^{2+}-NTA pull-down using His-tagged *Tb*IFT22 (WT and mutants) and untagged *Cr*IFT25/27/74/81. WT *Tb*IFT22 is able to pull down the *Cr* tetrameric complex, thus forming a chimeric IFT-B1 pentamer, while both the A86R and S19N mutant fail to bind the complex.

Source data are available online for this figure.

strong in the flagellum as also observed by kymograph analysis (Appendix Fig S6D). Finally, Immunofluorescence (IFA) showed that these cells display the classic distribution of IFT proteins. However, they assemble flagella of slightly shorter length (Appendix Fig S6E and F). Next, we addressed the question if the GTPase cycle plays a role during IFT in *T. brucei.* The IFT22$_{S19N}$ mutant is unable to bind GTP (Fig 1D) and displays weaker binding to IFT74/81 *in vitro* (Fig 4). A GFP-tagged RNAi-resistant version of
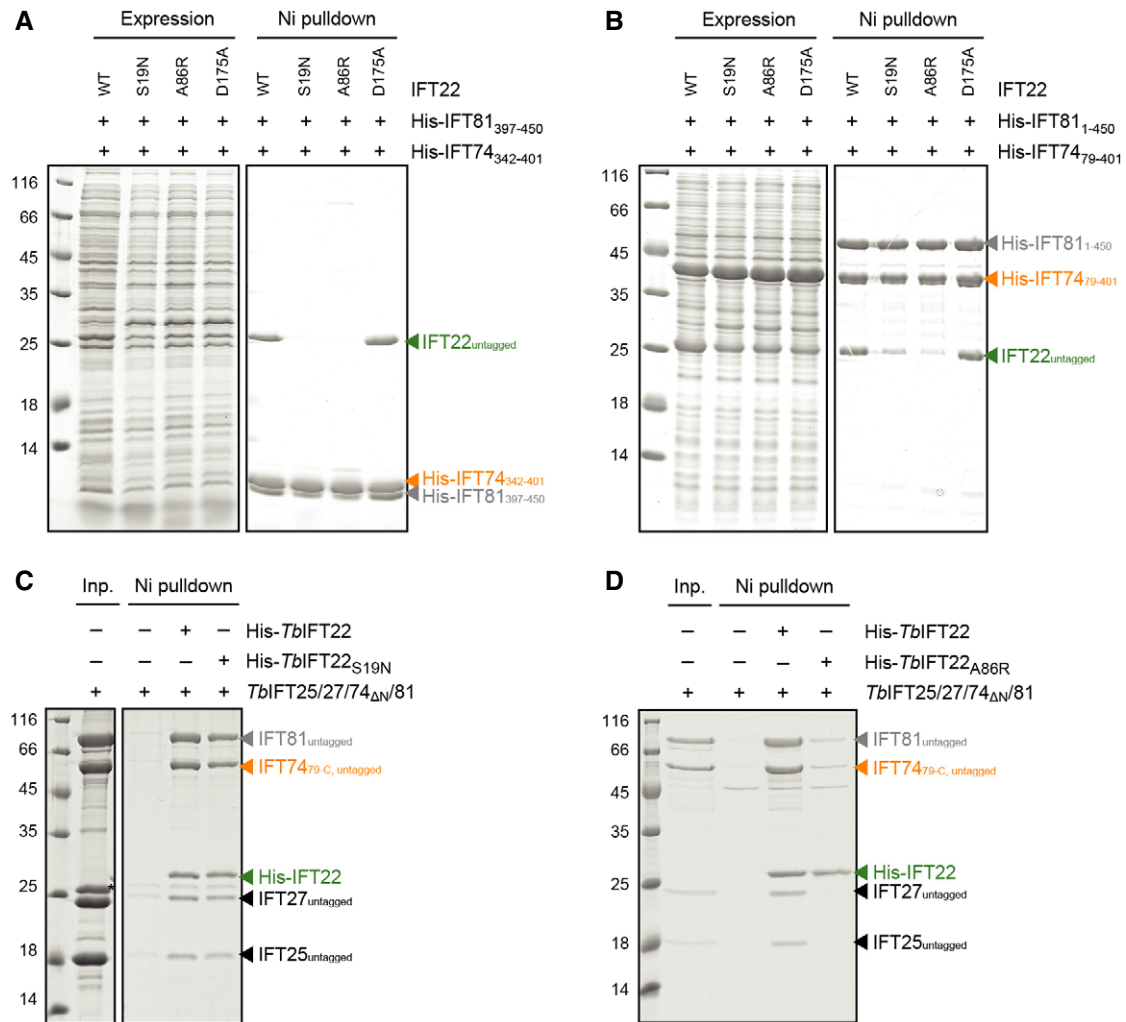
Figure 4. IFT74/81 interaction analysis using different IFT22 mutants.

A   SDS–PAGE gel of a Ni^{2+}-NTA pull-down using His-tagged $IFT74_{342-401}/81_{397-450}$ and untagged IFT22 (WT and mutants). Pull-downs were done from cell lysates of co-expressed proteins. Lanes 1–4 show similar total expression levels of the different co-expressed constructs (input samples). Lanes 5–8 show pull-down elutions. The $IFT22_{S19N}$ (inactive GTPase mutant) and the $IFT22_{A86R}$ mutant (IFT74/81-binding mutant) did not interact with the $IFT74_{342-401}/81_{397-450}$ complex in the pull-down experiment.

B   SDS–PAGE gel of a Ni^{2+}-NTA pull-down using the His-tagged $IFT74_{79-401}/81_{1-450}$ and untagged IFT22 (WT and mutants). Pull-downs were done from cell lysates of co-expressed proteins. Lanes 1–4 show similar total expression levels of the different co-expressed constructs (input samples). Lanes 5–8 show pull-down elutions. The $IFT22_{S19N}$ (inactive GTPase mutant) and the $IFT22_{A86R}$ mutant (IFT74/81-binding mutant) did not interact with the $IFT74_{79-401}/81_{1-450}$ complex in the pull-down experiment.

C   SDS–PAGE gel of a Ni^{2+}-NTA pull-down of full-length IFT25/27/74/81 complex with His-tagged IFT22 (WT and S19N mutant). The nucleotide-binding deficient mutant $IFT22_{S19N}$ interacts with IFT25/27/74/81 in the pull-down experiment.

D   SDS–PAGE gel of a Ni^{2+}-NTA pull-down of full-length IFT25/27/74/81 complex with His-tagged IFT22 (WT and A86R mutant). The IFT74/81-binding mutant $IFT22_{A86R}$ fails to pull down the full-length tetrameric complex.

Source data are available online for this figure.

$IFT22_{S19N}$ was expressed in trypanosomes. Western blot analysis confirmed efficient silencing of the endogenous IFT22 protein, whereas GFP-$IFT22_{S19N}$ remained present (Fig 5A). $IFT22_{S19N}$ was found at the base of the flagellum and trafficked normally within the organelle in the presence (Movie EV5) or the absence (Movie EV6) of endogenous IFT22, as formally demonstrated by kymograph analysis (Fig 5C). We noticed that IFT trains tended to pause and change speed more frequently in the latter case, suggesting a mild disruption of IFT. Although at first sight most cells looked normal, a minority of cells possessed clearly shorter flagella. This was

confirmed by IFA analysis with an axonemal marker (Fig 5B, second column, arrowheads) and some accumulation of IFT172 occurred in these cells (Fig 5B, last column). The length of the flagellum was measured and revealed that ~10% of the population had shorter flagella than normal (Fig 5D). Moreover, statistical analysis (Anova test) revealed a significant difference ($P < 0.001$) in the length of the flagellum between non-induced cells expressing $IFT22_{S19N}$ compared to the non-mutated version (Fig 5D). This indicates a dominant-negative effect of $IFT22_{S19N}$ on the length of the flagellum. This was also observed in induced conditions when
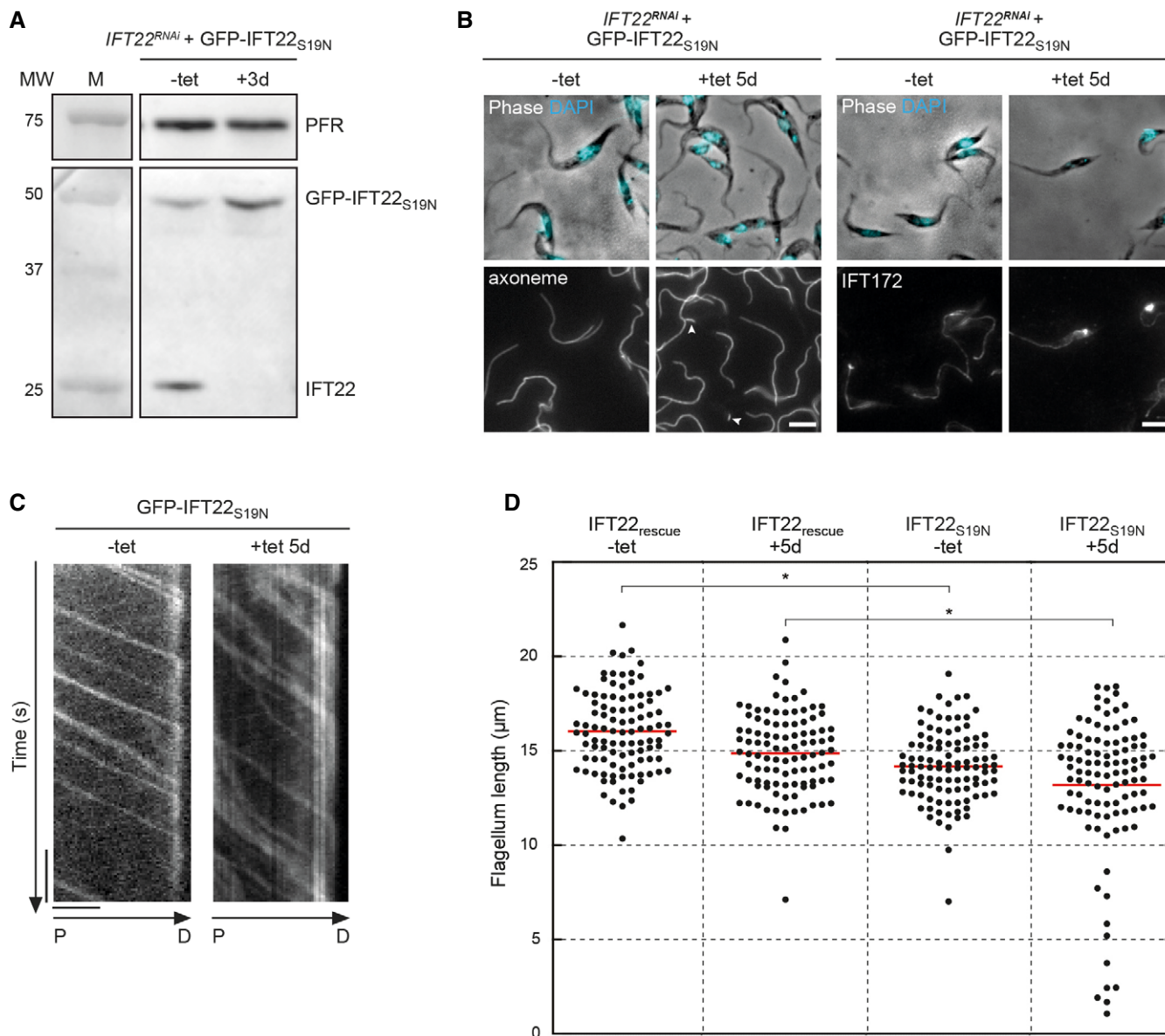
Figure 5. The IFT22$_{S19N}$ mutant shows a mild ciliogenesis phenotype *in vivo*.

A   Western blot analysis of the *IFT22^{RNAi} + GFP::IFT22$_{S19N}$* cell line probed with the anti-IFT22 antibody (bottom) and with an anti-paraflagellar rod (PFR) as loading control (top).

B   IFA of the indicated trypanosome cell lines using the mAb25 (marker for the axoneme, left panels) and an anti-IFT172 antibody (marker for IFT, right panels). The top panels show the phase contrast images merged with DAPI (cyan) that stains nuclear and mitochondrial DNA. Scale bars correspond to 5 μm.

C   Kymographs showing the movement of the GFP::IFT22$_{S19N}$ in the presence (left) or the absence (right) of the IFT22 endogenous protein. Note the improved signal-to-noise ratio in the absence of endogenous IFT22. P and D mark the proximal and distal ends of the flagellum, respectively. Scale bars are 5 s (time, vertical) and 5 μm (length, horizontal)

D   Dot plot representation of flagellum length in the indicated cell lines and conditions. For each condition, 100 flagella were measured and statistical analysis was performed with the ANOVA test. Significant differences are indicated with a star ($P < 0.0001$).

Source data are available online for this figure.

comparing with the IFT22 rescue cell line. From these results, we conclude that nucleotide binding by IFT22 is not an absolute requirement for IFT or flagellum construction in *T. brucei*, although minor perturbations of IFT and the formation of shorter flagella do suggest a somewhat impaired function of the IFT22$_{S19N}$ mutant compared to wild-type IFT22.

Association of IFT22 with IFT74/81 is essential for flagellum assembly in trypanosomes

To investigate if association of IFT22 with IFT74/81 is a requirement for IFT and flagellum construction in trypanosomes, we further investigated the *Tb*IFT22$_{A86R}$ mutant that was unable to assemble

into IFT22/74/81 core complexes (Fig 4A). TbIFT22$_{A86R}$ did not interact with TbIFT74$_{79-401}$/81$_{1-450}$ in pull-down experiments (Fig 4B). In case of the full-length TbIFT25/27/74/81 complex that still interacted with TbIFT22$_{S19N}$ (Fig 4C), the amount pulled down by TbIFT22$_{A86R}$ was close to background levels demonstrating that the IFT22$_{A86R}$-IFT74/81 interaction was severely impaired. We next investigated the consequences of the TbIFT22$_{A86R}$ mutation for flagellum formation *in vivo* in *T. brucei* cells. An RNAi-resistant version of GFP::IFT22 carrying the A86R mutation was expressed in trypanosomes in the tetracycline-inducible $IFT22^{RNAi}$ cell line. Western blot analysis showed the expected size for the fusion protein as well as efficient and specific silencing of the endogenous version of IFT22 (Fig 6A). In both non-induced and induced conditions (leading to knockdown of the endogenous IFT22 protein), TbIFT22$_{A86R}$ does not display IFT, fails to localize to the flagellum, and accumulates throughout the cytoplasm (Movies EV7 and EV8). Phase contrast microscopy showed the emergence of cells with tiny flagella filled with IFT172 protein or even no flagella (Fig 6B, last column). Transmission electron microscopy (TEM) analysis was performed on tetracycline-induced IFT22$_{rescue}$ and IFT22$_{A86R}$ cell lines. It revealed that the base of the flagellum was properly inserted in the flagellar pocket but that the flagella were very short and contained excessive amount of electron-dense material (Fig 6C, first two columns). The transition zone was properly assembled and displayed normal morphology (Fig 6C, third column) including the typical collarette that surrounds its proximal part (Trépout *et al*, 2018). By contrast, sections through the flagella revealed abnormal microtubule organization and excessive IFT material (Fig 6C, last two columns). This corresponds to the typical phenotype for *IFT22* RNAi silencing (Fig 6C, second row) (Adhiambo *et al*, 2009) and confirms that the IFT22$_{A86R}$ protein cannot rescue the phenotype. These results demonstrate that association of IFT22 with the IFT complex via IFT74/81 is crucial for proper flagellum organelle assembly in trypanosomes.

Discussion

Here we show that IFT22 specifically binds G-nucleotides through an unusual mechanism with μM affinity and has a low intrinsic GTP hydrolysis rate. GTP hydrolysis rates and affinities for nucleotides are comparable to the ones reported for IFT27, another small GTPase of the IFT complex (Bhogaraju *et al*, 2011), and indicate the need for a GAP, but not necessarily a GEF protein for realization of a complete GTPase cycle (Rensland *et al*, 1995; Vetter & Wittinghofer, 2001; Itzen & Goody, 2011). Studies in mouse and trypanosomes demonstrated that GTP-binding by IFT27 is needed for association with the IFT particle and that IFT27 mutants unable to bind GTP are excluded from the cilium (Eguether *et al*, 2014; Huet *et al*, 2014), suggesting that the IFT complex is an effector of IFT27. Interestingly, Eguether and colleagues found that the MmIFT27^{T19N} GTP-binding mutant retains some affinity for IFT-B in the absence of endogenous IFT27 and can enter the cilium and partially rescue the IFT27 knockout phenotype. These observations suggest that GTP-loading of IFT27 is not a strict requirement for IFT complex association but rather modulates the affinity of the interaction of IFT27 with IFT74/81. In sensory neurons of *C. elegans* worms, the IFT22$_{T42N}$ mutant

designed to preferentially bind GDP over GTP lost its ciliary localization and was delocalized through the cytoplasm (Schafer *et al*, 2006). As the IFT22$_{T42N}$ mutant was expressed in the presence of the endogenous IFT22 protein, the observed mis-localization of IFT22$_{T42N}$ could be a result of lower affinity for the IFT complex compared to the GTP-loaded wild-type version. Consistent with this, we observe that the GTP-binding by TbIFT22 is not strictly required for IFT complex formation but does appear to modulate TbIFT22-IFT74/81 complex formation. *In vitro* pull-down experiments suggest that GTP-bound TbIFT22 has higher affinity than the nucleotide-free TbIFT22$_{S19N}$ mutant for IFT74/81. The role of GTP hydrolysis by IFT27 and IFT22 (if any), possibly assisted by yet to be identified GAPs, remains to be identified.

Given that IFT22 co-purified with the IFT-B complex from trypanosomes (Franklin & Ullu, 2010), the phenotypic defect in retrograde transport upon RNAi knockdown was rather unexpected (Adhiambo *et al*, 2009). Here, we formally demonstrate that the phenotype is specific because it can be rescued by the expression of an RNAi-resistant version of the gene. Similar results were obtained for IFT25 and IFT27 that associate with the IFT-B complex and whose inhibition results in defects in entry of IFT dynein and IFT-A proteins in the trypanosome flagellum, possibly explaining the retrograde phenotype (Huet *et al*, 2014, 2019). The molecular basis for the retrograde IFT phenotype observed when IFT22 is knocked down or prevented from interacting with the IFT particle, and thus, entering the cilium is currently unknown although it is possible that IFT22, IFT25, and IFT27 cooperate in flagellum IFT dynein import. Curiously, IFT25 and IFT27 are not required for the construction of mouse primary cilia or cilia in the trachea (Keady *et al*, 2012; Eguether *et al*, 2014) but are essential for formation of the sperm flagellum (Liu *et al*, 2017; Zhang *et al*, 2017), suggesting that the requirement for some IFT proteins could be variable from one cell type to the other, even in the same organism. To our knowledge, the function of IFT22 has only been investigated in *T. brucei* and *C. elegans*. It will be interesting to see whether it behaves like IFT25/27 or more classic IFT proteins in mammalian cells.

IFT81 Short-Rib Polydactyly Syndrome mutation may affect IFT22 incorporation into the IFT complex

Although no patient mutations in IFT22 have been reported to date, a recent study identified a series of mutations in IFT81 causing Short-Rib Polydactyly Syndrome (SRPS) (Duran *et al*, 2016). One of the disease mutations reported was an in-frame deletion of amino acid L435, which corresponds to L443 in trypanosomes and is a well-conserved residue positioned directly in the interaction interface with IFT22 (Appendix Fig S7). L435 deletion could result in an overall IFT81 protein instability, but given its structural position and interaction with IFT22 residues (Appendix Fig S7) a likely molecular rationale for the observed ciliopathy phenotype is that the L435del leads to dissociation or weakened binding of IFT22 to IFT74/81. Unfortunately, no cultured cells were available for the L345del mutant and Duran and colleagues could thus not provide experimental data regarding expression levels and stability of this IFT81 mutant protein. Interestingly, many of the SRPS-causing mutations affect proteins required for retrograde IFT such as dynein-2 components (Dagoneau *et al*, 2009; Taylor *et al*, 2015) or the IFT-A
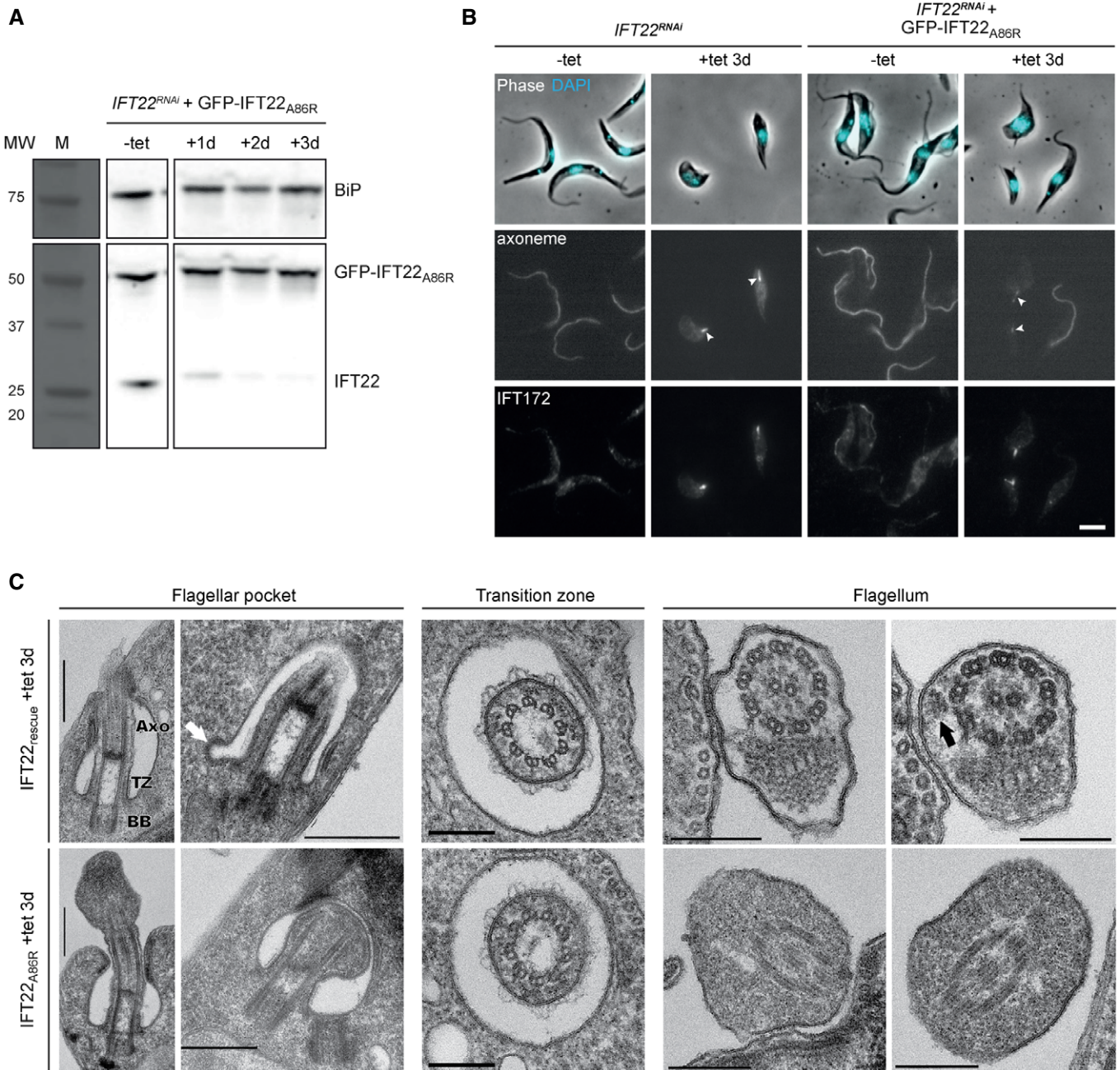
Figure 6. The IFT22$_{A86R}$ mutant displays a severe retrograde IFT phenotype *in vivo*.

A   Western blot analysis of the *IFT22^{RNAi}* + *GFP::IFT22$_{A86R}$* cell line probed with the anti-IFT22 antibody (bottom) and with an anti-BiP as loading control (top).

B   IFA with the indicated cell lines using the mAb25 (marker for the axoneme, central panels) and an anti-IFT172 antibody (marker for IFT, bottom panels). The top panels show the phase contrast images merged with DAPI (cyan) that stains nuclear and mitochondrial DNA. The arrowheads indicate the presence of short flagella stained with the Mab25 antibody in the *IFT22^{RNAi}* cells. Scale bars correspond to 5 μm.

C   Sections of *IFT22^{RNAi}* + *GFP::IFT22$_{rescue}$* (top panels) or *IFT22^{RNAi}* + *GFP::IFT22$_{A86R}$* cells (bottom panels) were analyzed by transmission electron microscopy. Sections through the flagellar pocket, the transition zone and the flagellum are shown. Scale bars are 500 nm (flagellar pocket sections) or 200 nm (transition zone and flagellum sections). The white arrow indicates an endocytic vesicle budding off the flagellar pocket, whereas the black one points at an IFT train. (Axo = axoneme, TZ = transition zone, BB = basal body).

Source data are available online for this figure.

component IFT121 (Mill *et al*, 2011), which result in retrograde IFT inactivation phenotypes. Intriguingly, knockdown of IFT22 in trypanosomes also causes a retrograde IFT phenotype (Adhiambo *et al*,

2009) consistent with the notion that weakened IFT22 association with the IFT complex could underlie the SRPS disease phenotypes observed in the patient with the IFT81 L345del mutation.

Materials and Methods

Recombinant protein expression and purification from *E. coli*

Wild-type and mutant (A86R, S19N, D175A/E) IFT22 proteins from *T. brucei* and *Mus musculus* were expressed as tobacco etch virus (TEV) cleavable N-terminal His_6 fusion proteins in *E. coli* BL21 (DE3) grown in TB-medium at 37°C. Overexpression was induced at 18°C at an OD_{600} of 1.8 with 0.5 mM IPTG. Cells were lysed by sonication in a buffer containing 50 mM Tris pH 7.5, 150 mM NaCl, 10% (v/v) glycerol, 10 mM imidazole, 2 mM $MgCl_2$, 5 mM β-mercaptoethanol, 1 mM PMSF, and 25 μg/ml DNaseI, and the extract was cleared by centrifugation (4°C, 75,000 *g*, 30 min). In a first step, proteins were purified via a Ni^{2+}-NTA affinity column (5 ml, Roche). In order to remove N-terminal His_6-tags, proteins were incubated with TEV protease overnight at room temperature and dialyzed against 50 mM NaCl buffer for subsequent ion-exchange chromatography (5 ml HiTrap Q sepharose, GE Healthcare). For further purification, proteins were subjected to size-exclusion chromatography (SEC) after concentrating to 20–30 mg/ml in a buffer containing 10 mM HEPES pH 7.5, 150 mM NaCl, 2 mM $MgCl_2$, and 1 mM DTT using a HiLoad Superdex 75 column (GE Healthcare). In general, both *Tb* and *Mm* (but not *Cr*) IFT22 were highly soluble and could be concentrated up to 2 mM (approx. 50 mg/ml). Proteins were stored at −80°C in SEC buffer. IFT22/74/81 core complexes of *Tb*, *Mm* and *Cr* as well as the N-terminal *Tb*IFT22/74$_{79-401}$/81$_{1-450}$ sub-complex were co-expressed in *E. coli* BL21(DE3) with each protein on a separate plasmid using N-terminal His_6-tagged IFT74 and IFT81 constructs and untagged IFT22. The same purification procedure was followed for IFT22. Expression and purification of *Cr*IFT25$_{1-136}$/27/74$_{128-C}$/81 was done as described previously (Taschner & Lorentzen, 2016a).

The *IFT74* sequence from extracted genomic trypanosome DNA contains an insertion corresponding to an additional 6 amino acids to the published sequence in the TriTrypDB database (Tb927.7.3370, 596 residues; Aslett *et al*, 2010) in the N-terminal part of the protein. This RPGSQM insertion is a repetitive sequence that is present in three consecutive copies in the annotated *Tb*IFT74 sequence, but in four copies in our *Tb*IFT74 construct. Since this part of the protein is predicted to be unstructured, we assume that this is a natural protein variant that does not affect IFT74 function. The IFT74 residue numbering in this publication will refer to this 602 residue-protein version.

Expression of selenomethionine derivatives

Selenomethionine derivative proteins were obtained from co-expression cultures of *Tb*IFT22/74$_{79-401}$/81$_{1-450}$ grown in M9 minimal medium supplemented with 60 mg/l selenomethionine. Overnight expression was induced at an OD_{600} of 1.0 with 0.5 mM IPTG, and the temperature was shifted to 20°C. The purification procedure was followed as for the native proteins.

Recombinant protein expression and purification from insect cells

Coding sequences of *Tb* IFT25, IFT27, IFT74$_{79-C}$, and IFT81 were cloned as TEV-cleavable N-terminal His_6 fusion proteins into the multiple cloning sites of pFL vectors, with IFT25/27 and IFT74$_{79-C}$/81

being located on the same vector, respectively (IFT27 into MCS1 via SmaI/SphI and IFT25 into MCS2 via EcoRI/XbaI; IFT81 into MCS1 via SmaI/SphI and IFT74 into MCS2 via EcoRI/XbaI). Recombinant baculoviruses were produced as described previously (Taschner *et al*, 2014). *Tb*IFT25/27 and *Tb*IFT74$_{79-C}$/81 heterodimeric complexes were co-expressed at 26°C in 6 l of HighFive insect cells (Invitrogen) infected with pre-determined amounts of recombinant viruses. Cells were harvested after 72 h and lysed by dounce homogenization in a buffer containing 20 mM HEPES pH 7.5, 250 mM sucrose, 10 mM KCl, 1.5 mM $MgCl_2$, 5 mM β-mercaptoethanol, and one pill of protease inhibitor cocktail (complete, EDTA-free, Roche). Nuclei were removed as described in Taschner *et al* (2016). Protein purification was done as outlined for proteins expressed in *E. coli*, except for using a HiLoad Superdex 200 or Superose 6 column in the SEC step.

Crystallization of GTP/GDP-*Tb*IFT22 and *Tb*IFT22/74$_{79-401}$/81$_{1-450}$

*Tb*IFT22 was set up for crystallization at 15.2 mg/ml in SEC buffer by sitting-drop vapor diffusion in 0.2 μl drops obtained by mixture of equal volumes of protein and crystallization solution. Crystals appeared after 2 days at 4°C as fine needle clusters after mixing with 20% (w/v) PEG3350, 50 mM NaCacodylate pH 6.5, and 200 mM calcium acetate and turned into three-dimensional hexagons over the course of 10 days. No excess of GTP was added to the protein or the crystallization solution since *Tb*IFT22 was purified bound to GTP from *E. coli*. For crystallization of the GDP-loaded state, refolded nucleotide-free *Tb*IFT22 was set up at 15.6 mg/ml in SEC buffer supplemented with 7 mM GDP by sitting-drop vapor diffusion in 0.2 μl drops obtained by mixture of equal volumes of protein and crystallization solution. Crystals grew with a similar shape transition as described above at 4°C after mixing with 15% (w/v) PEG6000, 50 mM NaCacodylate pH 7.0, and 200 mM CaAcetate. Both GTP- and GDP-*Tb*IFT22 crystals were cryoprotected in mother liquor containing 15% (v/v) glycerol prior to flash freezing in liquid nitrogen. Crystals of the *Tb*IFT22/74/81 complex (native and selenomethionine derivate, Appendix Fig S3C) were obtained from protein concentrated to 25 mg/ml by sitting-drop vapor diffusion at 4°C in 0.2 μl drops (0.1 μl protein solution containing 2 mM GTP + 0.1 μl crystallization solution) supplemented with 40 nl freshly prepared microseeds. Crystals grew after mixing with 15% (v/v) glycerol, 7.5% (w/v) PEG4000, and 100 mM HEPES pH 7.5 and were cryoprotected in reservoir solution containing 33% (v/v) ethylene glycol prior to flash freezing in liquid nitrogen.

Data collection and crystal structure determination

For the structures of the small GTPase, diffraction data were collected at the PXIII (for GTP-*Tb*IFT22) and PXII (for GDP-*Tb*IFT22) beamline at the Swiss Light Source (SLS) in Villigen, Switzerland, and were processed with XDS (Kabsch, 2010) prior to scaling with Aimless of the CCP4 package (Winn *et al*, 2011). The structure of GTP-*Tb*IFT22 was solved at 2.3 Å resolution by molecular replacement (MR) with an ensemble of three different superposed Rab GTPases found by HHpred search (PDB IDs: 1vg8, 2y8e, 3oes) using the program Phaser (Storoni *et al*, 2004). The asymmetric unit contained two molecules of IFT22 and analysis with Xtriage detected twinned data. The model was completed by iterative cycles of model building in COOT (Emsley *et al*, 2010), followed by refinement in

PHENIX (Adams *et al*, 2010) using NCS restraints and applying the twin law h, -h-k, -l. The GDP-*Tb*IFT22 structure was determined at 2.5 Å resolution using the previously solved GTP-bound structure as a search model for MR. X-ray diffraction data for the *Tb*IFT22/74/81 complex structure were collected at the PXII beamline at SLS, indexed with XDS, and scaled with the CCP4 program Aimless. The structure was determined from selenomethionine substituted protein crystals. Single anomalous dispersion data were recorded at the Se peak wavelength, and AUTOSOL as part of the PHENIX package was used to locate Se sites and calculate experimental phases and electron density. The structure was modeled and refined at 3.2 Å resolution from a dataset derived from a selenomethionine substituted protein crystal, since native crystals diffracted significantly worse. Two copies of the $TbIFT22/74_{79-401}/81_{1-450}$ complex are present in the asymmetric unit. The 3.2 Å model was built in COOT and refined in PHENIX using NCS and secondary structure restraints. The two copies were very similar in most parts, but showed significant conformational differences in the C-terminal IFT22-binding coiled-coils of IFT74/81 (ccVI). While we could build IFT22 into the electron density map of one copy of the complex, we were unable to build IFT22 with confidence in the second copy of the complex. Data collection and refinement statistics are summarized in Table 1.

Affinity pull-down experiments

For purified proteins, Ni^{2+}-NTA affinity beads were pre-incubated with buffer containing 150 mM NaCl, 50 mM Tris pH 7.5, 2 mM $MgCl_2$, and 10 mM imidazole. 40 μg of purified His-tagged proteins was bound to 30 μl of beads in a total volume of 500 μl at 4°C. After 1 h, beads were washed twice with 1 ml buffer to remove excess protein and were incubated with 400 μg of untagged interaction partner in 500 μl total volume for another hour. Beads were washed three times with 1 ml buffer to remove unbound protein. Bound proteins were eluted from the beads with 50 μl buffer containing 500 mM imidazole. In the case of Ni^{2+} pull-downs from cell lysates, the proteins were co-expressed from separate plasmids in *E. coli* BL21(DE3) cells. 20 μl of each culture was taken and supplemented with SDS loading dye as "total expression samples". Cell pellets from 10 ml overnight culture were resuspended in 1.5 ml lysis buffer (50 mM Tris pH 7.5, 150 mM NaCl, 10% (v/v) glycerol, 10 mM imidazole, 2 mM $MgCl_2$), and cells were lysed by sonication (1 min, 1 s pulse/1 s pause). Cell extracts were cleared by centrifugation (4°C, 16,000 *g*, 30 min), and the supernatant was incubated at 4°C with 20 μl Ni^{2+}-NTA affinity beads pre-incubated with lysis buffer. After 1 h, beads were washed three times with 1 ml buffer and bound proteins were eluted with 50 μl buffer containing 500 mM imidazole. Eluate contents were analyzed by SDS–PAGE.

Protein denaturation by urea and refolding for nucleotide removal

*Tb*IFT22 and the *Tb*IFT22/74/81 core complex were refolded in order to remove bound GTP, since more gentle methods such as EDTA or SAP treatment were not successful (Appendix Fig S1B). Proteins were diluted to 0.5 mg/ml and dialyzed in a dialysis tube against buffer containing 50 mM Tris pH 7.5, 150 mM NaCl, 10% (v/v) glycerol, and 8 M urea overnight at 4°C. After 18 h, dialysis tubes were transferred to fresh buffer without urea for protein refolding and dialyzed for another 24 h. The buffer was exchanged twice to remove residual urea. After refolding, proteins were concentrated and subjected to SEC. Successful nucleotide removal was verified by HPLC.

HPLC nucleotide analysis

Nucleotide species of purified proteins and their hydrolysis states were verified at 20°C by reversed phase high-performance liquid chromatography (HPLC) using a Vydac 218TP C_{18} column with a Securityguard filter cartridge system (Phenomenex) attached. Nucleotides were separated by isocratic elution at 20°C with a buffer composed of 100 mM potassium phosphate pH 6.5, 10 mM tetra-butylammonium bromide, and 7.5% (v/v) acetonitrile and elution detected at 254 nm.

Nucleotide-binding experiments

Nucleotide affinities of *Tb*IFT22 (WT, mutants, and core complex) were determined by fluorescence spectrophotometric measurements (PerkinElmer LS50B) of 2′(3′)-O-(*N*-methylanthraniloyl)-labeled (mant-labeled) nucleotides (Jena Bioscience). Increasing concentrations (2–200 μM) of nucleotide-free protein (confirmed by HPLC) were incubated with 1 μM mant-GDP/-GMPPNP/-ADP/-AMPPNP for 30 min in a buffer containing 50 mM Tris pH 7.5, 100 mM NaCl, and 5 mM $MgCl_2$ in 60 μl volumes. Emission spectra of the samples were monitored at 20°C in a quartz cuvette from 400–500 nm (excitation at 355 nm). Intrinsic protein fluorescence and mant-nucleotide background fluorescence were substracted from the data. Emission maxima of the mant fluorophore at 448 nm were plotted against protein concentrations. Curve fitting and dissociation constant (K_d) determination was done with GraphPad Prism 6.0 software using a binding equation that describes a single-site binding model.

GTPase assay

GTPase activities of *Tb*IFT22 and the *Tb*IFT22/74/81 core complex were measured at 20°C with the EnzChek Phosphate Assay Kit (ThermoFisher). Reactions were initiated by adding 1 mM GTP to the protein mixed with kit solutions according to the manufacturer's recommendations. The release of inorganic phosphate (P_i) upon GTP hydrolysis followed by an enzymatic reaction was monitored over 20 min. The change in absorption at 360 nm was detected every minute using a PerkinElmer Lambda19 UV spectrometer. As a negative control, intrinsic GTP hydrolysis in buffer was followed. Rate quantifications were done with the help of a linear standard curve for P_i generated with defined concentrations of KH_2PO_4 from 10 μM to 200 μM after 20-min incubation.

Trypanosome cultures and transfection

Procyclic *T. brucei* cell lines were derivatives of the strain 427, grown in SDM79 medium containing 10% fetal calf serum and hemin (Brun & Schönenberger, 1979). Generation of the inducible $IFT22^{RNAi}$ ($RABL5^{RNAi}$) cell line has been described previously

(Adhiambo *et al*, 2009). In this cell line, a 447-nucleotide long fragment of *IFT22* was cloned in the pZJM vector (Wang *et al*, 2000). The two T7 promoters face each other and can be induced in the presence of tetracycline, leading to the production of double-stranded RNA (dsRNA). To express RNAi-resistant versions of IFT22, the entire nucleotide sequence of IFT22 was modified by substituting the last and when possible the second nucleotide of the codon to render the transcript insensitive to RNAi (Huet *et al*, 2014) hence retaining the original amino acid sequence. The construct was tagged with GFP, and the resulting plasmid was called pPCPFReGFPIFT22^{RNAiRes}. GeneCust Europe carried out the chemical synthesis, and additional point mutations were introduced to generate the S19N, A86R, and D175A versions. The plasmids were linearized with NsiI to target integration in the *PFR2* locus (Adhiambo *et al*, 2009) following transfection using the Nucleofector Technology (Lonza, Italy; Burkard *et al*, 2007).

Immunofluorescence

Cultured cells were spun at $580 \times g$ to remove the supernatant and then washed in SDM79 medium without serum. Cells were spread onto poly-L-lysine-coated slides, dehydrated, and fixed in methanol at $-20°C$ for 5 min. Slides were rehydrated in $1\times$ phosphate-buffered saline (PBS) for 15 min. Primary antibodies were diluted in PBS + 0.1% bovine serum albumin (BSA), and slides were incubated for 60 min at 37°C. The mAb25 mouse monoclonal antibody that recognizes the TbSAXO1 protein found along the entire length of the axoneme (Pradel *et al*, 2006) was used as a flagellar marker. The anti-IFT22/RABL5 is a polyclonal mouse antiserum recognizing IFT22 (Adhiambo *et al*, 2009), and the monoclonal anti-IFT172 antibody is a classic marker for IFT-B proteins (Absalon *et al*, 2008). Slides were washed three times in PBS before incubation with specific secondary antibodies, diluted in PBS + 0.1% BSA, for 60 min at 37°C. Sub-class specific secondary antibodies were used for double labeling and detection. Secondary antibodies were coupled to either Cy3 or Cy5 (Jackson ImmunoResearch Laboratories, West Grove, PA) or Alexa 488 (Invitrogen). Slides were washed again and stained with DAPI (2 μg/μl; stains nucleus and kinetoplast) and mounted using ProLong (Invitrogen). Experiments performed at least twice to confirm the results.

A DMI4000 Leica microscope equipped with a 100× 1.4 lens (Leica, Germany) was used for observing slides, and images were captured using an ORCA-03G camera (Hamamatsu). Images were analyzed using ImageJ v1.49 (National Institutes of Health, USA). Flagellum length was measured using the mAb25 signal and the measuring tool of ImageJ. A total of 50 (*Tb*IFT22$_{D175A}$; Appendix Fig S6F) or 100 (*Tb*IFT22$_{S19N}$; Fig 5D) flagella were measured per experiment. Populations were compared using the ANOVA test with the appropriate tool in Kaleidagraph 4.5.2 (Synergy Software).

Live cell imaging

Cultured cells were spread onto a slide, covered with a coverslip, and observed using the DMI4000 Leica Microscope. Videos were acquired using an Evolve 512 EMCCD Camera (Photometrics, AZ) driven by the Micro-Manager Acquisition software (Molecular Probes, CA) to record videos at 100-ms exposure. Analysis of acquired videos was performed using ImageJ v1.49. Kymograph

extraction was performed using the KymographTracker plugin in Icy 1.9.5.1 (BioImage Analysis Unit, Institut Pasteur, France). Kymographs give a 2D graphical representation of the spatial position of IFT trains over time. The *x*-axis corresponds to the length of the region of interest (ROI), while the *y*-axis corresponds to the elapsed time. The ROI was traced semi-automatically as a path in a maximum intensity enhanced projection of a time-lapse image sequence (200 frames at 10 fps) by clicking control points in the intensity projection such that the curve followed a high pixel-value trail.

Transmission electron microscopy

For TEM, cells were treated essentially as in Fort *et al* (2016). Cells were directly fixed in suspension with 2.5% (final) glutaraldehyde and washed in PBS, and the pellet was post-fixed for one hour with 2.5% EM grade glutaraldehyde and 1% paraformaldehyde containing 0.1% tannic acid. The samples were washed three times in phosphate buffer for 5 min, and the pellet was resuspended in 1% osmium tetroxide in phosphate buffer. After 1 h, the pellet was rinsed five times with water and incubated overnight at 4°C in 2% uranyl acetate. It was rinsed five times in water before graded dehydration series in acetone (10–30–50–70–90–100% for 15 min each). Graded replacement with the Agar-100 resin was then carried out (25–50–75–100% for 15 min each) followed by three successive incubation in 100% Agar-100. The resin was polymerized for 2 h at 100°C. Ultrathin sections (50–70 nm thick) were collected on formvar/carbon-coated nickel grids using a Leica EM UC6 ultra-microtome and stained with uranyl acetate (2%, w/v) (uranyl acetate dihydrate, Electron Microscopy Sciences) and lead citrate (80 mM, buffer made in-house). Observations were made on a Tecnai BioTWIN 120 cryo electron microscope (FEI), and images were captured with a MegaView II camera (Arecont Vision, France) and processed with AnalySIS and Adobe Photoshop CS4 (San Jose, CA).

Western blot

Cells were washed once in PBS. Laemmli loading buffer was added to the cells, and samples were boiled for 5 min. 20 μg of protein was loaded onto each lane of a Criterion™ XT Bis-Tris Precast Gel 4–12% (Bio-Rad, UK) for SDS–PAGE separation. XT-Mops (1×) diluted in deionized water was used as a running buffer. Proteins were either transferred onto nitrocellulose membranes at 100 V over 1 h or by using the Bio-Rad Trans-Blot Turbo™ blotting system (25 V over 7 min). The membrane was blocked with 5% skimmed milk for one hour and then incubated with the anti-RABL5/IFT22 primary antibody diluted in 0.05% PBS-Tween (PBST). The anti-RABL5 polyclonal antibody was diluted 1/500. As a loading control, the anti-BiP (marker for an endoplasmic reticulum protein; Bangs *et al*, 1993) diluted 1/1,000 and anti-PFR (L13D6; Kohl *et al*, 1999) diluted 1/50 were used. Both primary antibodies were diluted in 0.05% PBST containing 1% milk. After primary antibody incubation, three washes of 5 min each were performed in 0.05% PBST followed by secondary antibody incubation. Anti-mouse secondary antibody coupled to horseradish peroxidase, diluted 1/20,000 in 0.05% PBST containing 1% milk, was used, and the membrane was incubated for 1 h. The Amersham ECL Western Blotting Detection Reagent Kit (GE Healthcare Life Sciences, UK) was used for final detection of proteins on the membrane.

Accession numbers

Acknowledgements

Author contributions

Conflict of interest

References

Absalon S, Blisnick T, Kohl L, Toutirais G, Doré G, Julkowska D, Tavenet A, Bastin P (2008) Intraflagellar transport and functional analysis of genes required for flagellum formation in trypanosomes. *Mol Biol Cell* 19: 929–944

Adams PD, Afonine PV, Bunkóczi G, Chen VB, Davis IW, Echols N, Headd JJ, Hung L-W, Kapral GJ, Grosse-Kunstleve RW, McCoy AJ, Moriarty NW, Oeffner R, Read RJ, Richardson DC, Richardson JS, Terwilliger TC, Zwart PH (2010) PHENIX: a comprehensive Python-based system for macromolecular structure solution. *Acta Crystallogr D Biol Crystallogr* 66: 213–221

Adhiambo C, Blisnick T, Toutirais G, Delannoy E, Bastin P (2009) A novel function for the atypical small G protein Rab-like 5 in the assembly of the trypanosome flagellum. *J Cell Sci* 122: 834–841

Alushin GM, Ramey VH, Pasqualato S, Ball DA, Grigorieff N, Musacchio A, Nogales E (2010) The Ndc80 kinetochore complex forms oligomeric arrays along microtubules. *Nature* 467: 805–810

Alva V, Nam S-Z, Söding J, Lupas AN (2016) The MPI bioinformatics Toolkit as an integrative platform for advanced protein sequence and structure analysis. *Nucleic Acids Res* 44: W410–W415

Aslett M, Aurrecoechea C, Berriman M, Brestelli J, Brunk BP, Carrington M, Depledge DP, Fischer S, Gajria B, Gao X, Gardner MJ, Gingle A, Grant G, Harb OS, Heiges M, Hertz-Fowler C, Houston R, Innamorato F, Iodice J, Kissinger JC *et al* (2010) TriTrypDB: a functional genomic resource for the Trypanosomatidae. *Nucleic Acids Res* 38: D457–D462

Bangs JD, Uyetake L, Brickman MJ, Balber AE, Boothroyd JC (1993) Molecular cloning and cellular localization of a BiP homologue in *Trypanosoma brucei*. Divergent ER retention signals in a lower eukaryote. *J Cell Sci* 105 (Pt. 4): 1101–1113

Bhogaraju S, Taschner M, Morawetz M, Basquin C, Lorentzen E (2011) Crystal structure of the intraflagellar transport complex 25/27. *EMBO J* 30: 1907–1918

Bhogaraju S, Cajanek L, Fort C, Blisnick T, Weber K, Taschner M, Mizuno N, Lamla S, Bastin P, Nigg EA, Lorentzen E (2013a) Molecular basis of tubulin transport within the cilium by IFT74 and IFT81. *Science* 341: 1009–1012

Bhogaraju S, Engel BD, Lorentzen E (2013b) Intraflagellar transport complex structure and cargo interactions. *Cilia* 2: 10

Blacque OE, Li C, Inglis PN, Esmail MA, Ou G, Mah AK, Baillie DL, Scholey JM, Leroux MR (2006) The WD repeat-containing protein IFTA-1 is required for retrograde intraflagellar transport. *Mol Biol Cell* 17: 5053–5062

Blacque OE, Scheidel N, Kuhns S (2018) Rab GTPases in cilium formation and function. *Small GTPases* 9: 76–94

Brun R, Schönenberger M (1979) Cultivation and in vitro cloning or procyclic culture forms of *Trypanosoma brucei* in a semi-defined medium. Short communication. *Acta Trop* 36: 289–292

Burkard G, Fragoso CM, Roditi I (2007) Highly efficient stable transformation of bloodstream forms of *Trypanosoma brucei*. *Mol Biochem Parasitol* 153: 220–223

Ciferri C, Pasqualato S, Screpanti E, Varetti G, Santaguida S, Dos Reis G, Maiolica A, Polka J, De Luca JG, De Wulf P, Salek M, Rappsilber J, Moores CA, Salmon ED, Musacchio A (2008) Implications for kinetochore-microtubule attachment from the structure of an engineered Ndc80 complex. *Cell* 133: 427–439

Cole DG, Chinn SW, Wedaman KP, Hall K, Vuong T, Scholey JM (1993) Novel heterotrimeric kinesin-related protein purified from sea urchin eggs. *Nature* 366: 268–270

Cole DG, Diener DR, Himelblau AL, Beech PL, Fuster JC, Rosenbaum JL (1998) Chlamydomonas kinesin-II-dependent intraflagellar transport (IFT): IFT particles contain proteins required for ciliary assembly in *Caenorhabditis elegans* sensory neurons. *J Cell Biol* 141: 993–1008

Dagoneau N, Goulet M, Geneviève D, Sznajer Y, Martinovic J, Smithson S, Huber C, Baujat G, Flori E, Tecco L, Cavalcanti D, Delezoide A-L, Serre V, Le Merrer M, Munnich A, Cormier-Daire V (2009) DYNC2H1 mutations cause asphyxiating thoracic dystrophy and short rib-polydactyly syndrome, type III. *Am J Hum Genet* 84: 706–711

van Dam TJP, Townsend MJ, Turk M, Schlessinger A, Sali A, Field MC, Huynen MA (2013) Evolution of modular intraflagellar transport from a coatomer-like progenitor. *Proc Natl Acad Sci USA* 110: 6943–6948

Duran I, Taylor SP, Zhang W, Martin J, Forlenza KN, Spiro RP, Nickerson DA, Bamshad M, Cohn DH, Krakow D (2016) Destabilization of the IFT-B cilia core complex due to mutations in IFT81 causes a spectrum of short-rib polydactly syndrome. *Sci Rep* 6: 34232

Eguether T, San Agustin JT, Keady BT, Jonassen JA, Liang Y, Francis R, Tobita K, Johnson CA, Abdelhamed ZA, Lo CW, Pazour GJ (2014) IFT27 links the BBSome to IFT for maintenance of the ciliary signaling compartment. *Dev Cell* 31: 279–290

Emmer BT, Maric D, Engman DM (2010) Molecular mechanisms of protein and lipid targeting to ciliary membranes. *J Cell Sci* 123: 529–536

Emsley P, Lohkamp B, Scott WG, Cowtan K (2010) Features and development of Coot. *Acta Crystallogr D Biol Crystallogr* 66: 486–501

Espinosa EJ, Calero M, Sridevi K, Pfeffer SR (2009) RhoBTB3: a Rho GTPase-family ATPase required for endosome to Golgi transport. *Cell* 137: 938–948

Follit JA, Xu F, Keady BT, Pazour GJ (2009) Characterization of mouse IFT complex B. *Cell Motil Cytoskeleton* 66: 457–468

Fort C, Bonnefoy S, Kohl L, Bastin P (2016) Intraflagellar transport is required for the maintenance of the trypanosome flagellum composition but not its length. *J Cell Sci* 129: 3026–3041

Franklin JB, Ullu E (2010) Biochemical analysis of PIFTC3, the *Trypanosoma brucei* orthologue of nematode DYF-13, reveals interactions with established and putative intraflagellar transport components. *Mol Microbiol* 78: 173–186

Holm L, Sander C (1993) Protein structure comparison by alignment of distance matrices. *J Mol Biol* 233: 123–138

Huangfu D, Liu A, Rakeman AS, Murcia NS, Niswander L, Anderson KV (2003) Hedgehog signalling in the mouse requires intraflagellar transport proteins. *Nature* 426: 83–87

Huet D, Blisnick T, Perrot S, Bastin P (2014) The GTPase IFT27 is involved in both anterograde and retrograde intraflagellar transport. *Elife* 3: e02419

Huet D, Blisnick T, Perrot S, Bastin P (2019) IFT25 is required for the construction of the trypanosome flagellum. *J Cell Sci* 132: jcs228296

Ishikawa H, Ide T, Yagi T, Jiang X, Hirono M, Sasaki H, Yanagisawa H, Wemmer KA, Stainier DY, Qin H, Kamiya R, Marshall WF (2014) TTC26/DYF13 is an intraflagellar transport protein required for transport of motility-related proteins into flagella. *Elife* 3: e01566

Itzen A, Goody RS (2011) GTPases involved in vesicular trafficking: structures and mechanisms. *Semin Cell Dev Biol* 22: 48–56

Kabsch W (2010) XDS. *Acta Crystallogr D Biol Crystallogr* 66: 125–132

Kanie T, Abbott KL, Mooney NA, Plowey ED, Demeter J, Jackson PK (2017) The CEP19-RABL2 GTPase complex binds IFT-B to initiate intraflagellar transport at the ciliary base. *Dev Cell* 42: 22–36.e12

Keady BT, Samtani R, Tobita K, Tsuchya M, San Agustin JT, Follit JA, Jonassen JA, Subramanian R, Lo CW, Pazour GJ (2012) IFT25 links the signal-dependent movement of Hedgehog components to intraflagellar transport. *Dev Cell* 22: 940–951

Kohl L, Sherwin T, Gull K (1999) Assembly of the paraflagellar rod and the flagellum attachment zone complex during the *Trypanosoma brucei* cell cycle. *J Eukaryot Microbiol* 46: 105–109

Kohl L, Robinson D, Bastin P (2003) Novel roles for the flagellum in cell morphogenesis and cytokinesis of trypanosomes. *EMBO J* 22: 5336–5346

Kozminski KG, Johnson KA, Forscher P, Rosenbaum JL (1993) A motility in the eukaryotic flagellum unrelated to flagellar beating. *Proc Natl Acad Sci USA* 90: 5519–5523

Landau M, Mayrose I, Rosenberg Y, Glaser F, Martz E, Pupko T, Ben-Tal N (2005) ConSurf 2005: the projection of evolutionary conservation scores of residues on protein structures. *Nucleic Acids Res* 33: W299–W302

Langousis G, Hill KL (2014) Motility and more: the flagellum of *Trypanosoma brucei*. *Nat Rev Microbiol* 12: 505–518

Leung DW, Rosen MK (2005) The nucleotide switch in Cdc42 modulates coupling between the GTPase-binding and allosteric equilibria of Wiskott-Aldrich syndrome protein. *Proc Natl Acad Sci USA* 102: 5685–5690

Liu H, Li W, Zhang Y, Zhang Z, Shang X, Zhang L, Zhang S, Li Y, Somoza AV, Delpi B, Gerton GL, Foster JA, Hess RA, Pazour GJ, Zhang Z (2017) IFT25, an

intraflagellar transporter protein dispensable for ciliogenesis in somatic cells, is essential for sperm flagella formation. *Biol Reprod* 96: 993–1006

Lo JCY, Jamsai D, O'Connor AE, Borg C, Clark BJ, Whisstock JC, Field MC, Adams V, Ishikawa T, Aitken RJ, Whittle B, Goodnow CC, Ormandy CJ, O'Bryan MK (2012) RAB-like 2 has an essential role in male fertility, sperm intra-flagellar transport, and tail assembly. *PLoS Genet* 8: e1002969

Lucker BF, Behal RH, Qin H, Siron LC, Taggart WD, Rosenbaum JL, Cole DG (2005) Characterization of the intraflagellar transport complex B core: direct interaction of the IFT81 and IFT74/72 subunits. *J Biol Chem* 280: 27688–27696

Mill P, Lockhart PJ, Fitzpatrick E, Mountford HS, Hall EA, Reijns MAM, Keighren M, Bahlo M, Bromhead CJ, Budd P, Aftimos S, Delatycki MB, Savarirayan R, Jackson IJ, Amor DJ (2011) Human and mouse mutations in WDR35 cause short-rib polydactyly syndromes due to abnormal ciliogenesis. *Am J Hum Genet* 88: 508–515

Mourão A, Nager AR, Nachury MV, Lorentzen E (2014) Structural basis for membrane targeting of the BBSome by ARL6. *Nat Struct Mol Biol* 21: 1035–1041

Nishijima Y, Hagiya Y, Kubo T, Takei R, Katoh Y, Nakayama K (2017) RABL2 interacts with the intraflagellar transport-B complex and CEP19 and participates in ciliary assembly. *Mol Biol Cell* 28: 1652–1666

Paduch M, Jeleń F, Otlewski J (2001) Structure of small G proteins and their regulators. *Acta Biochim Pol* 48: 829–850

Pazour GJ, Dickert BL, Witman GB (1999) The DHC1b (DHC2) isoform of cytoplasmic dynein is required for flagellar assembly. *J Cell Biol* 144: 473–481

Pazour GJ, Dickert BL, Vucica Y, Seeley ES, Rosenbaum JL, Witman GB, Cole DG (2000) Chlamydomonas IFT88 and its mouse homologue, polycystic kidney disease gene tg737, are required for assembly of cilia and flagella. *J Cell Biol* 151: 709–718

Pazour GJ, Agrin N, Leszyk J, Witman GB (2005) Proteomic analysis of a eukaryotic cilium. *J Cell Biol* 170: 103–113

Piperno G, Mead K (1997) Transport of a novel complex in the cytoplasmic matrix of Chlamydomonas flagella. *Proc Natl Acad Sci USA* 94: 4457–4462

Porter ME, Bower R, Knott JA, Byrd P, Dentler W (1999) Cytoplasmic dynein heavy chain 1b is required for flagellar assembly in Chlamydomonas. *Mol Biol Cell* 10: 693–712

Pradel LC, Bonhivers M, Landrein N, Robinson DR (2006) NIMA-related kinase TbNRKC is involved in basal body separation in *Trypanosoma brucei*. *J Cell Sci* 119: 1852–1863

Prevo B, Mangeol P, Oswald F, Scholey JM, Peterman EJG (2015) Functional differentiation of cooperating kinesin-2 motors orchestrates cargo import and transport in *C. elegans* cilia. *Nat Cell Biol* 17: 1536–1545

Qin H, Wang Z, Diener D, Rosenbaum J (2007) Intraflagellar transport protein 27 is a small G protein involved in cell-cycle control. *Curr Biol* 17: 193–202

Ralston KS, Kabututu ZP, Melehani JH, Oberholzer M, Hill KL (2009) The *Trypanosoma brucei* flagellum: moving parasites in new directions. *Annu Rev Microbiol* 63: 335–362

Reiter JF, Leroux MR (2017) Genes and molecular pathways underpinning ciliopathies. *Nat Rev Mol Cell Biol* 18: 533–547

Rensland H, John J, Linke R, Simon I, Schlichting I, Wittinghofer A, Goody RS (1995) Substrate and product structural requirements for binding of nucleotides to H-ras p21: the mechanism of discrimination between guanosine and adenosine nucleotides. *Biochemistry* 34: 593–599

Rosenbaum JL, Witman GB (2002) Intraflagellar transport. *Nat Rev Mol Cell Biol* 3: 813–825

Rotureau B, Ooi C-P, Huet D, Perrot S, Bastin P (2014) Forward motility is essential for trypanosome infection in the tsetse fly. *Cell Microbiol* 16: 425–433

Salinas RY, Pearring JN, Ding J-D, Spencer WJ, Hao Y, Arshavsky VY (2017) Photoreceptor discs form through peripherin-dependent suppression of ciliary ectosome release. *J Cell Biol* 216: 1489–1499

San Agustin JT, Pazour GJ, Witman GB (2015) Intraflagellar transport is essential for mammalian spermiogenesis but is absent in mature sperm. *Mol Biol Cell* 26: 4358–4372

Schafer JC, Winkelbauer ME, Williams CL, Haycraft CJ, Desmond RA, Yoder BK (2006) IFTA-2 is a conserved cilia protein involved in pathways regulating longevity and dauer formation in *Caenorhabditis elegans*. *J Cell Sci* 119: 4088–4100

Scheffzek K, Ahmadian MR (2005) GTPase activating proteins: structural and functional insights 18 years after discovery. *Cell Mol Life Sci* 62: 3014–3038

Schneider L, Clement CA, Teilmann SC, Pazour GJ, Hoffmann EK, Satir P, Christensen ST (2005) PDGFRalphaalpha signaling is regulated through the primary cilium in fibroblasts. *Curr Biol* 15: 1861–1866

Serricchio M, Schmid AW, Steinmann ME, Sigel E, Rauch M, Julkowska D, Bonnefoy S, Fort C, Bastin P, Bütikofer P (2015) Flagellar membranes are rich in raft-forming phospholipids. *Biol Open* 4: 1143–1153

Sievers F, Wilm A, Dineen D, Gibson TJ, Karplus K, Li W, Lopez R, McWilliam H, Remmert M, Söding J, Thompson JD, Higgins DG (2011) Fast, scalable generation of high-quality protein multiple sequence alignments using Clustal Omega. *Mol Syst Biol* 7: 539

Signor D, Wedaman KP, Orozco JT, Dwyer ND, Bargmann CI, Rose LS, Scholey JM (1999) Role of a class DHC1b dynein in retrograde transport of IFT motors and IFT raft particles along cilia, but not dendrites, in chemosensory neurons of living *Caenorhabditis elegans*. *J Cell Biol* 147: 519–530

Silva DA, Huang X, Behal RH, Cole DG, Qin H (2012) The RABL5 homolog IFT22 regulates the cellular pool size and the amount of IFT particles partitioned to the flagellar compartment in *Chlamydomonas reinhardtii*. *Cytoskeleton (Hoboken)* 69: 33–48

Simon I, Zerial M, Goody RS (1996) Kinetics of interaction of Rab5 and Rab7 with nucleotides and magnesium ions. *J Biol Chem* 271: 20470–20478

Slep KC, Vale RD (2007) Structural basis of microtubule plus end tracking by XMAP215, CLIP-170, and EB1. *Mol Cell* 27: 976–991

Stenmark H (2009) Rab GTPases as coordinators of vesicle traffic. *Nat Rev Mol Cell Biol* 10: 513–525

Storoni LC, McCoy AJ, Read RJ (2004) Likelihood-enhanced fast rotation functions. *Acta Crystallogr D Biol Crystallogr* 60: 432–438

Taschner M, Bhogaraju S, Vetter M, Morawetz M, Lorentzen E (2011) Biochemical mapping of interactions within the intraflagellar transport (IFT) B core complex: IFT52 binds directly to four other IFT-B subunits. *J Biol Chem* 286: 26344–26352

Taschner M, Bhogaraju S, Lorentzen E (2012) Architecture and function of IFT complex proteins in ciliogenesis. *Differentiation* 83: S12–S22

Taschner M, Kotsis F, Braeuer P, Kuehn EW, Lorentzen E (2014) Crystal structures of IFT70/52 and IFT52/46 provide insight into intraflagellar transport B core complex assembly. *J Cell Biol* 207: 269–282

Taschner M, Lorentzen E (2016a) Recombinant reconstitution and purification of the IFT-B core complex from *Chlamydomonas reinhardtii*. *Methods Mol Biol* 1454: 69–82

Taschner M, Lorentzen E (2016b) The intraflagellar transport machinery. *Cold Spring Harb Perspect Biol* 8: 1–19

Taschner M, Weber K, Mourão A, Vetter M, Awasthi M, Stiegler M, Bhogaraju S, Lorentzen E (2016) Intraflagellar transport proteins 172, 80, 57, 54, 38, and 20 form a stable tubulin-binding IFT-B2 complex. *EMBO J* 35: 773–790

Taylor SP, Dantas TJ, Duran I, Wu S, Lachman RS, University of Washington Center for Mendelian Genomics Consortium, Nelson SF, Cohn DH, Vallee RB, Krakow D (2015) Mutations in DYNC2LI1 disrupt cilia function and cause short rib polydactyly syndrome. *Nat Commun* 6: 7092

Trépout S, Tassin A-M, Marco S, Bastin P (2018) STEM tomography analysis of the trypanosome transition zone. *J Struct Biol* 202: 51–60

Uthaiah RC, Praefcke GJK, Howard JC, Herrmann C (2003) IIGP1, an interferon-gamma-inducible 47-kDa GTPase of the mouse, showing cooperative enzymatic activity and GTP-dependent multimerization. *J Biol Chem* 278: 29336–29343

Vetter IR, Wittinghofer A (2001) The guanine nucleotide-binding switch in three dimensions. *Science* 294: 1299–1304

Wang Z, Morris JC, Drew ME, Englund PT (2000) Inhibition of *Trypanosoma brucei* gene expression by RNA interference using an integratable vector with opposing T7 promoters. *J Biol Chem* 275: 40174–40179

Winn MD, Ballard CC, Cowtan KD, Dodson EJ, Emsley P, Evans PR, Keegan RM, Krissinel EB, Leslie AGW, McCoy A, McNicholas SJ, Murshudov GN, Pannu NS, Potterton EA, Powell HR, Read RJ, Vagin A, Wilson KS (2011) Overview of the CCP4 suite and current developments. *Acta Crystallogr D Biol Crystallogr* 67: 235–242

Zhang Y, Liu H, Li W, Zhang Z, Shang X, Zhang D, Li Y, Zhang S, Liu J, Hess RA, Pazour GJ, Zhang Z (2017) Intraflagellar transporter protein (IFT27), an IFT25 binding partner, is essential for male fertility and spermiogenesis in mice. *Dev Biol* 432: 125–139